Towards Integrated Silicon Photonic Architectures for Quantum Information Processing

by

Uttara Chakraborty

S.B., Massachusetts Institute of Technology (2017)

Submitted to the Department of Electrical Engineering and Computer Science
in partial fulfillment of the requirements for the degree of

Master of Science in Electrical Engineering and Computer Science

at the

MASSACHUSETTS INSTITUTE OF TECHNOLOGY

June 2019

Signature redacted

Signature of Author .....
Department of Electrical Engineering and Computer Science
May 23, 2019

Signature redacted

Certified by .....
Dirk Robert Englund
Associate Professor of Electrical Engineering and Computer Science
Thesis Supervisor

Signature redacted

Accepted by .....
Leslie A. Kolodziejski
Professor of Electrical Engineering and Computer Science
Chair, Department Committee on Graduate Students

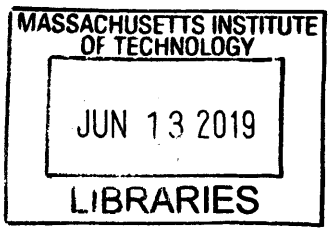

ARCHIVES

Towards Integrated Silicon Photonic Architectures for Quantum Information Processing

by

Uttara Chakraborty

Submitted to the Department of Electrical Engineering and Computer Science
on May 23, 2019 in Partial Fulfillment of the
Requirements for the Degree of Master of Science in
Electrical Engineering and Computer Science

ABSTRACT

Silicon photonics is a highly-promising platform for on-chip quantum information processing. Linear optical quantum computing architectures necessitate the implementation of integrated single photon sources, passive and active optics, and single photon detectors. This thesis presents the development of a scalable, real-time feedback control protocol for stabilizing microring resonator frequencies in parallel with quantum computation using the same classical pump laser fields as are used to seed photon generation. The feedback protocol is applied to correct static and dynamic errors in silicon microring resonators due to fabrication variations and ambient fluctuations, and to demonstrate high-visibility two-photon quantum interference with photon pairs generated by spontaneous four wave mixing. Progress on a new interferometrically-coupled photon generation device for four-photon quantum interference is also presented. Finally, a new scheme is proposed for non-volatile phase shifters in large-scale photonic integrated circuits. The potential use of shape-memory materials for straining silicon waveguides to induce refractive index shifts is explored through finite-element simulations.

Thesis Supervisor: Dirk Robert Englund
Title: Associate Professor of Electrical Engineering and Computer Science

Acknowledgments

I am grateful to my supervisor Professor Dirk Englund for his exemplary guidance and inspiration. Thanks to Dr. Jacques Carolan who has been an outstanding mentor to me, and also to Rui Tang for being an awesome collaborator on the four-photon source project. And I owe much to all the members of the Quantum Photonics Group. I am grateful to Professor Isaac Chuang and to Professor Jing Kong for their advice and encouragement. I remain indebted to Professor Leslie Kolodziejski for her unstinting support, as well as to the EECS Graduate Office. A special thank you to Janice Balzer for her constant support. The work presented in this thesis has been supported by my NDSEG Fellowship.

Contents

List of Figures

Chapter 1

Introduction

As the end of Moore's Law looms on the horizon and transistors reach the limit of miniaturization, the paradigm of quantum computing holds great promise for meeting the challenge of our ever-increasing demands for computational power. Nature, at its most fundamental level, is governed by the laws of quantum mechanics. Quantum systems can be described by states comprised of superpositions of qubits, or quantum bits. Additionally, states can be entangled such that parts of a large system are correlated in a manner inexplicable by classical physics. By exploiting the inherent superposition and entanglement properties of the quantum realm, quantum computers can parallelize operations and lead to immense speedups in information processing.

Many physical systems have been explored for the implementation of qubits, including solid-state memories such as quantum dots and color centers [1, 2], photons, superconducting circuits, and trapped ions. This work focuses on photonic quantum computing architectures, where qubits are encoded in the polarization states of photons. Photons' lack of interaction with the environment leads to zero-decoherence and the ability to transmit information over long distances. Photons are not restricted to nearest-neighbor interactions and can be easily manipulated easily via waveguides in CMOS-compatible platforms, enabling the marriage of integrated silicon technologies with the paradigm of linear optical quantum computing and paving the way for the development of scalable, integrated silicon photonic systems for quantum information

processing [46].

This thesis focuses on two crucial components of an integrated silicon photonic platform for optical quantum computing: single photon sources and phase shifters. Chapter 2 gives an overview of the building blocks of silicon quantum computing architectures and their principles of operation, and highlights the state of the art. In Chapter 3, we address the problem of correcting errors in single photon sources in real-time. Using a pair of integrated microring resonator single photon sources, we demonstrate an *in situ* feedback-based control technique to stabilize the ring resonances in the presence of environmental fluctuations and device crosstalk. We apply our technique to generate two-photon quantum interference with high visibility. Chapter 4 summarizes progress on an ongoing effort to generate truly unentangled photon pairs using a new interferometrically-coupled photon generation ring architecture and demonstrate four-photon quantum interference. Finally, in Chapter 5 we turn our attention to non-volatile phase shifters for minimizing energy consumption in large scale photonic integrated circuits. To this end, we propose the use of shape-memory materials to strain silicon waveguides and effect phase shifts via the photoelastic effect; in addition, we consider the potential of shape-memory materials to induce a second order nonlinearity in silicon.

Chapter 2

Optical quantum computing

Linear optical quantum computing was born in 2000 when Knill, Laflamme and Millburn proved that universal quantum computers can be built using only linear optics, single photons, and photon detectors [43, 47]. Photonic qubits are encoded in the path degree of freedom, in what is known as the "dual rail" encoding scheme. A qubit consists of a photon spread between two spatial modes, which correspond to the modes of a single-mode waveguide in integrated optics. A general qubit is represented as

$$cos(\theta/2)|0\rangle + sin(\theta/2)e^{i\phi}|1\rangle.$$

Rotations of the qubit around the Bloch sphere are implemented with Mach-Zehnder interferometers and phase shifters, as will be described in the following sections. Quantum photonic states are represented in the Fock basis $|n_1, n_2, ..., n_k\rangle$ where n_i is the number of photons in a given spatial mode i [47].

2.1 Silicon photonic integrated circuits

Silicon provides a highly promising platform for CMOS-compatible manufacturing and integration of photonics [46]. While glass-based waveguide technologies [6] have been demonstrated to accomplish high-fidelity quantum operations, there is little

promise of their scalability and suitability for circuits of increasing complexity, given that even simple circuits require devices as large as 10 cm. Silicon is an excellent candidate for photonics for many of the same reasons that it has dominated electronics manufacturing–it is abundant, mechanically robust, can be easily doped or made extremely pure, and has high thermal conductivity. Additionally, silicon's intrinsic third order ($\chi^{(3)}$) nonlinearity–100 times higher than that of glass–renders it a natural candidate for photon generation. Silicon waveguides, on the other hand, with their high refractive index contrast between the silicon core (n_{Si} = 3.48) and silicon dioxide cladding (n_{SiO_2}=1.45), enable the fabrication of ultra-compact, tightly-confining devices. Standard silicon-on-insulator (SOI) waveguides are typically fabricated in wafers consisting of a 220 nm thick silicon device layer with a 2 μm buried oxide layer below and an oxide cladding layer above; for telecom C-band operation at wavelengths around 1550 nm, single mode waveguides with a 220 nm x 500 nm silicon waveguide core and 5 μm bend radii are commonly used to enable a very high device integration density. Losses, mainly arising from sidewall roughness, tend to be low–around 3 dB/cm. Most of the building blocks needed for on-chip quantum information processing have individually been demonstrated in the silicon-on-insulator platform, but there still remain many outstanding challenges to improving device performance for achieve low photon loss and reliably scaling up to integrate several hundred thousands of components on chip. Fig. 2.1 provides a conceptual example of how the different components required for on-chip quantum information processing can be integrated together. The following sections give an overview of selected key components of an integrated silicon photonic quantum information processing platform.

2.1.1 Single photon sources

Optical quantum computing–unlike quantum key distribution which encodes information in one single photon at a time–requires bursts of photons, which cannot be approximated by attenuated laser light [47]. While atom-like systems like quantum dots and solid-state color centers emit truly single photons, photon pairs can be pro-

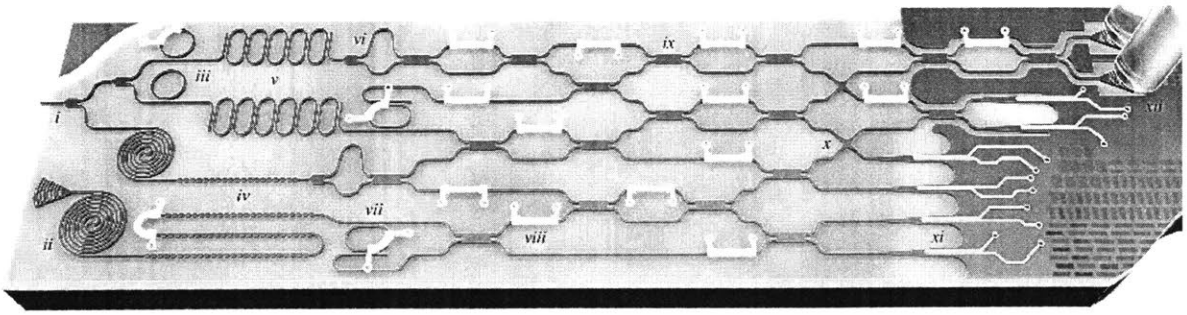

Figure 2.1: Mock-up of an integrated quantum photonic device with single photon sources, filters, passive and active optics, and single photon detectors. Adapted from [46].

duced by the nonlinear optical process of spontaneous four wave mixing (SFWM) in silicon, thanks to silicon's large $\chi^{(3)}$. In non-degenerate SFWM (Fig 2.2: left), two photons from a bright pump laser are converted to a signal photon at a higher frequency and an idler photon at a lower frequency such that energy is conserved [50]:

$$2\omega_{pump} = \omega_{signal} + \omega_{idler} \tag{2.1}$$

In degenerate SFWM (Fig. 2.2: right), photons of two different pump frequencies

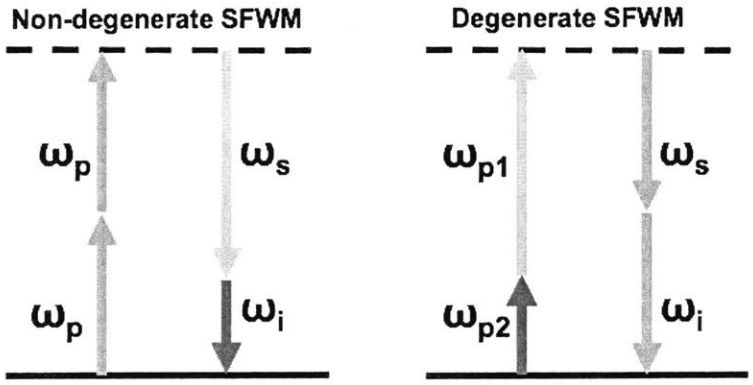

Figure 2.2: Non-degenerate (left) and degenerate (right) spontaneous four wave mixing. $\omega_{p(1,2)}$, ω_s, ω_i denote pump, signal and idler frequencies respectively.

are converted to two photons of the same frequency, which by energy conservation is

the average of the pump frequencies:

$$\omega_{pump1} + \omega_{pump2} = 2\omega_{signal,idler} \tag{2.2}$$

Spontaneous four wave mixing results in a "heralded" single photon source, where the detection of one photon heralds the presence of the other in the pair. An ideal heralded single photon source should be efficient, needing low pump powers for photon pair generation. The probability of generating more than one pair must be low, and the heralding efficiency must be high (given the detection of an idler photon, the signal must exit the source with high probability). Furthermore, the photons in a pair must be unentangled in all degrees of freedom in order to achieve high purity of the single photons [47].

Simple straight waveguides or spiral waveguides can be used for pair generation, although they lead to low SFWM efficiency. The photon generation rate R for a straight waveguide pumped by a continuous wave (CW) laser is given by

$$R = \frac{P^2 L^2 \gamma^2 \Delta v}{2} \tag{2.3}$$

where P is the pump power, L the length of the waveguide, γ the nonlinear coupling constant (proportional to $\chi^{(3)}$ and inversely proportional to the effective modal area), and Δv the filter bandwidth for separating the pump from the generated photons [47]. In reality, at high pump powers, the nonlinear effects of two-photon absorption and free carrier absorption can inhibit the quadratic rise in generation rate with pump power, causing the rate to saturate. To improve upon the SFWM efficiency, the pump power could be increased, but this has the drawback of added noise and harder separation of pump and signal idler photons. In addition, the photons generated in a waveguide are highly entangled in frequency, which is undesirable for pure heralded photon sources. To minimize correlations between photons in a pair, the pump bandwidth must exceed the filter bandwidth; since a high filter bandwidth is necessary for a high photon generation rate, obtaining decorrelated photons in a photon pair

would require exceedingly short pump pulses.

Resonant structures, such as ring resonators (Fig. 2.3) [45], provide an alternative architecture to circumvent the above problems with SFWM in waveguides. The pair generation rate R for a ring resonator coupled to a bus waveguide and pumped by a CW laser is given by

$$R = P^2\gamma^2 v_g \frac{L}{4}\frac{t^8}{(1-r\tau)^7} \tag{2.4}$$

where P is the pump power, L the length of the waveguide, γ the nonlinear coupling constant, v_g the group velocity in the ring; t, r, and τ are the bus-to-ring coupling, bus-to-bus coupling, and ring round trip amplitude transmission coefficients respectively [47]. Taking into account the probability of each of the photons escaping the ring per round trip, the net pair generation output rate is given by

$$R_{net} = P^2\gamma^2 v_g \frac{L}{4}\frac{(1-r^2)^6}{(1-r\tau)^7(1-r^2\tau^2)^2} \tag{2.5}$$

Compared to straight or spiral waveguides, the smaller footprint of ring resonators enables a higher device integration density. The circulating pump intensity is increased when the pump is evanescently coupled from a bus waveguide into a ring resonator, reducing the need for higher input pump power to achieve a large pair generation rate. A ring resonator requires the pump to be aligned with one of the ring resonances for SFWM, and enforces the generation of photons at frequencies aligning with neighboring resonance of the ring. That is, if a ring is pumped at frequency ω_p, signal and idler photons will be generated symmetrically at the $+N^{th}$ and $-N^{th}$ resonances of the ring, conserving energy (see schematic in Fig. 2.4) and making it easier to separate the pump from the signal and idler photons by filtering. With narrower filter bandwidths, a pulsed laser can also be used to provide a larger pump bandwidth, resulting in decreased spectral correlations between photons in a pair and paving the way for high-purity heralded sources [47].

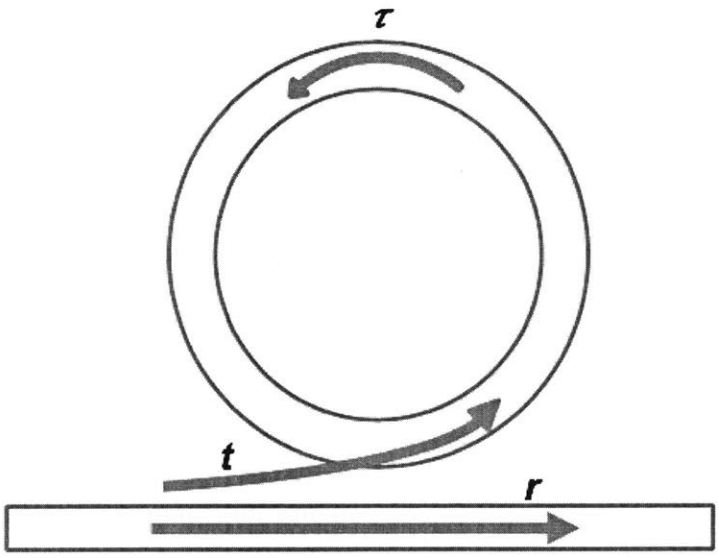

Figure 2.3: Ring resonator photon source. t, r, and τ are the bus-to-ring coupling, bus-to-bus coupling, and ring round trip amplitude transmission coefficients respectively.

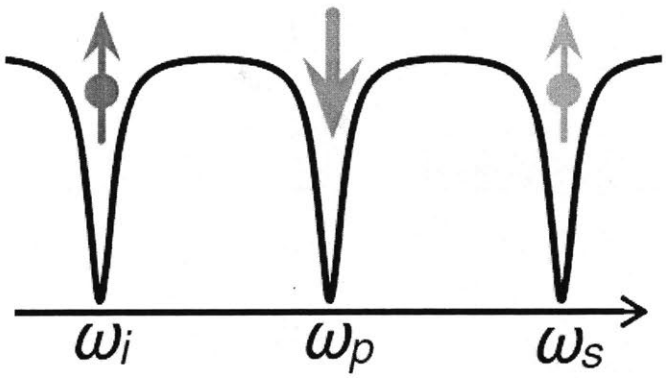

Figure 2.4: Spontaneous four wave mixing in a ring resonator, where the pump, signal and idler frequencies align with resonances of the ring. Adapted from [5].

2.1.2 Passive optical elements

Once photons have been generated, they can be manipulated with passive linear optical components. Complex networks of hundreds of components such as directional couplers and Mach Zehnder interferometers have been demonstrated in the silicon-on-insulator platform, and can provide a scalable way to engineer multi-photon quantum interference for large-scale quantum information processing. Recent progress in the field on engineering on-chip quantum interference and entanglement will be discussed in Section 2.2. Here, we give an overview of the mechanics of the directional coupler (an integrated beamsplitter) and the Mach Zehnder interferometer, as used in our experiments in Chapters 3 and 4 to demonstrate on-chip quantum interference.

The directional coupler [4], shown in Fig. 2.5, is defined by the following transfer matrix [47]:

$$S = \begin{bmatrix} \sqrt{R} & i\sqrt{T} \\ i\sqrt{T} & \sqrt{R} \end{bmatrix} \tag{2.6}$$

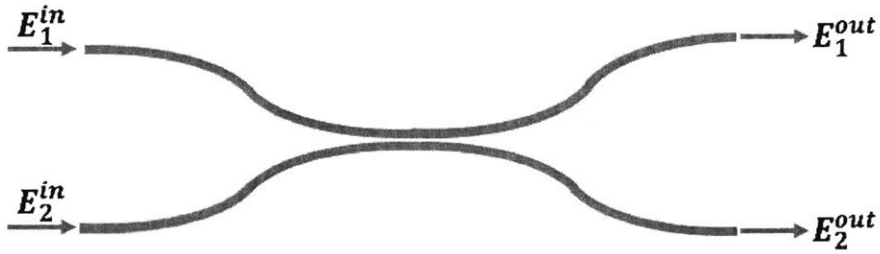

Figure 2.5: Directional coupler.

In the case of perfect 50-50 splitting, $R{=}T{=}\frac{1}{2}$, resulting in the simplified transfer matrix given by

$$S = \frac{1}{\sqrt{2}} \begin{bmatrix} 1 & i \\ i & 1 \end{bmatrix} \tag{2.7}$$

For a Mach-Zehnder interferometer [4] consisting of a directional coupler concatenated with a phase shift applied to one output followed by another directional coupler

as shown in Fig. 2.6, the transfer matrix is given by

$$S = \frac{1}{2}\begin{bmatrix} 1 & i \\ i & 1 \end{bmatrix}\begin{bmatrix} e^{i\theta} & 0 \\ 0 & 1 \end{bmatrix}\begin{bmatrix} 1 & i \\ i & 1 \end{bmatrix} \tag{2.8}$$

$$= ie^{i\frac{\theta}{2}}\begin{bmatrix} sin\frac{\theta}{2} & cos\frac{\theta}{2} \\ cos\frac{\theta}{2} & -sin\frac{\theta}{2} \end{bmatrix} \tag{2.9}$$

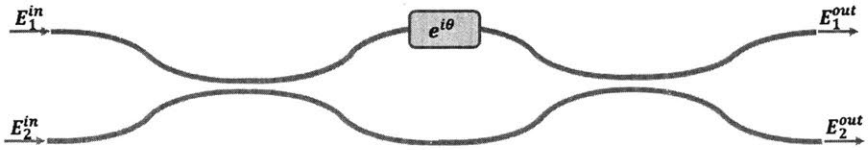

Figure 2.6: Mach-Zehnder interferometer with a phase shift of θ on the top arm.

In the following section, we will consider the effect of directional couplers on a few representative input photon states.

2.1.3 Phase shifters

Phase shifters are essential to optical quantum computing for implementing path-encoded qubits and generating interference with Mach-Zehnder interferometers. A phase shifter operates by changing the effective refractive index of the waveguide material over a region of a certain length, leading to the transmitted light's acquiring a relative phase compared to light passing through a phase-shifter-less region of the same length. The change in phase is given by

$$\Delta\phi = \frac{2\pi\Delta n_{eff}L}{\lambda} \tag{2.10}$$

To achieve a phase shift of π volts, which corresponds to a full switching of light from one arm of a Mach-Zehnder to another, a the length of the required phase shifter is given by

$$L_\pi = \frac{\lambda}{2\Delta n_{eff}} \tag{2.11}$$

An integrated phase shifter, the equivalent of a bulk-optic wave plate, can be implemented using several different architectures, including doped silicon heaters based on the thermo-optic and plasma dispersion effects [66], MEMS-based switches [65], and electro-optic modulators [8]. In this work, our chips use doped silicon thermo-optic phase shifters based on the design in [25], which has a V_π of 4.36 V and consumes $\sim$ 25 mW per π phase shift over a length of $\sim$62 μm. In Chapter 5 we explore a new approach to implementing non-volatile integrated phase shifters using the shape-memory properties of certain ceramics and alloys.

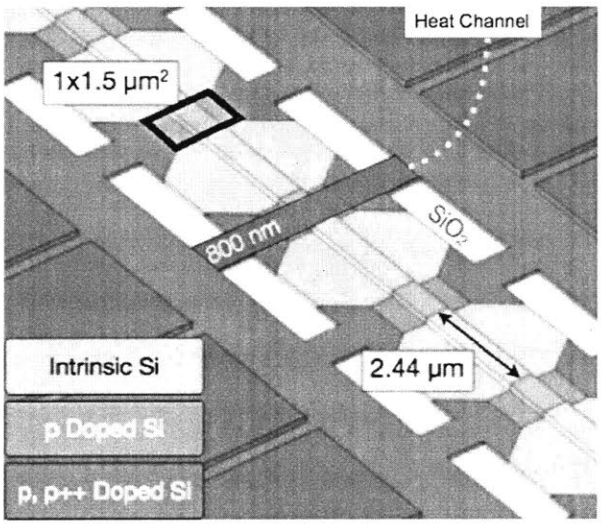

Figure 2.7: Doped-silicon thermo-optic phase shifter. Adapted from [25].

2.2 On-chip quantum interference

By using single photon sources, directional couplers, Mach-Zehnder interferometers, and phase shifters, we can create and manipulate quantum states of light [47]. For example, when two indistinguishable photons enter a directional coupler with one photon at each input port (with input modes a and b), the input state is given by

$$|\Psi_{\text{in}}\rangle = |11\rangle = a^\dagger b^\dagger |00\rangle. \tag{2.12}$$

The output state (with output modes c and d) is:

$$|\Psi_{\text{out}}\rangle = \left(\sqrt{R}c^\dagger + i\sqrt{T}d^\dagger\right) + \left(\sqrt{R}d^\dagger + i\sqrt{T}c^\dagger\right)|\text{vac}\rangle \tag{2.13}$$

$$= \left[i\sqrt{RT}\left(c^{\dagger 2} + d^{\dagger 2}\right) + c^\dagger d^\dagger (R-T)\right]|\text{vac}\rangle \tag{2.14}$$

$$= i\sqrt{2RT}\left(|20\rangle_{cd} + |02\rangle_{cd}\right) + (R-T)|11\rangle_{cd} \tag{2.15}$$

For a balanced coupler with R=T=$\frac{1}{2}$, the probability of detecting a coincidence–one photon at each output–vanishes, and both photons are guaranteed to exit at the same port. However, if one photon acquires a phase relative to the other, the coincidence probability is non-zero, as illustrated in Fig. 2.8 from the original Hong-Ou-Mandel paper ([61]).

Quantum interference on a silicon photonic integrated circuit has been demonstrated in [50], where path-entangled photon pairs generated by SFWM in two spiral waveguides were interfered on-chip to yield high-visibility two-photon coincidence fringes. More recently, on-chip quantum interference with SFWM photon pairs generated in independent ring resonators has been demonstrated to yield four-photon coincidence fringes [48].

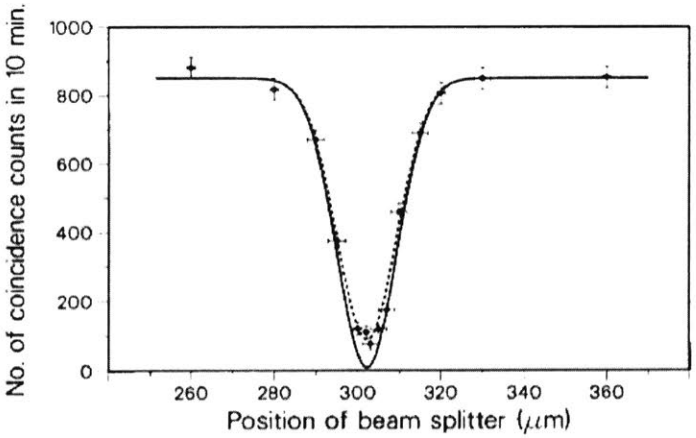

Figure 2.8: Hong-Ou-Mandel interference. Adapted from [61].

Chapter 3

Feedback control of single photon sources

Precise control of individual qubits is essential to the performance of large-scale quantum information processing systems. Drifts in the system due to unavoidable environmental fluctuations, thermal noise, etc. can lead to errors in individual qubits over time, necessitating the development of optimal control techniques to continuously track and compensate for parameter drift-induced errors on the fly. To address error correction in large-scale qubit arrays, such control techniques must be scalable and allow for the correction of arbitrarily large numbers of qubits in parallel. While methods for pre-characterizing circuitry via classical laser fields have been developed [12, 13], finding techniques for active real-time monitoring of errors remains a challenge. To achieve parameter drift compensation, previous work in the field of superconducting quantum computing has demonstrated a feedback-based "adaptive detection event parameter tuning" technique that scales as O(1) with the size of the system [14]. Here, we present an *in situ* control technique for photonic quantum computing that monitors and corrects errors in silicon microring resonator single photon sources without making destructive measurements on the quantum state of the system. Errors in resonator frequencies are diagnosed and corrected in parallel with the optical quantum computation using the same classical laser fields used for photon

generation and in a manner that can be scaled up to large numbers of qubits. We achieve sub-1 pm microring resonance stabilization in the presence of environmental fluctuations and successfully demonstrate the feedback-controlled quantum state engineering. This chapter is based on the work in [49].

3.1 Quantum state engineering device

As described in Chapter 2, silicon microring resonators are a leading platform for ultra-bright and pure single photon generation via spontaneous four-wave mixing (SFWM). In large-scale quantum information processing architectures, many microring resonators must be tuned to the same frequency. Precise alignment and stability of the resonators is essential for ensuring the indistinguishability of photons and generating quantum interference, and their brightness and efficiency as single photon sources scales with their quality factors. In this experiment, we use the standard CMOS foundry-fabricated SOI photonic device shown in Fig. 3.1 below, containing four microring resonators and five thermo-optic phase shifters within an area of 0.08 mm^2.

Two microring resonators with a radius of 11 μm are used for photon pair generation. These rings have a linewidth of $\Delta\lambda = 60$ pm, a resonance quality factor of $Q \approx 2.5 \times 10^4$ (Fig. 3.2), and a free spectral range (FSR) of 8.8 nm. The device architecture corresponds to five sequential stages (see Fig. 1) that result in the production of correlated photon pairs by the inverse Hong-Ou-Mandel effect. First, two pumps of different frequencies ω_{p_1} and ω_{p_2} are mixed on a 50-50 directional coupler. Then, the mixed pumps couple to the two generation rings to produce photon pairs by spontaneous four wave mixing. These signal and idler photon pairs are generated at the frequency that is the average of the two pump frequencies: $\omega_{s,i} = (\omega_{p_1} + \omega_{p_2})/2$. The microring resonators are coupled to bus waveguides that are 500 nm wide x 200 nm high that convey the generated photons forward. After a distance of 40 μm, the bus waveguides couple to demultiplexing microring resonators of radius 8 nm and FSR 12

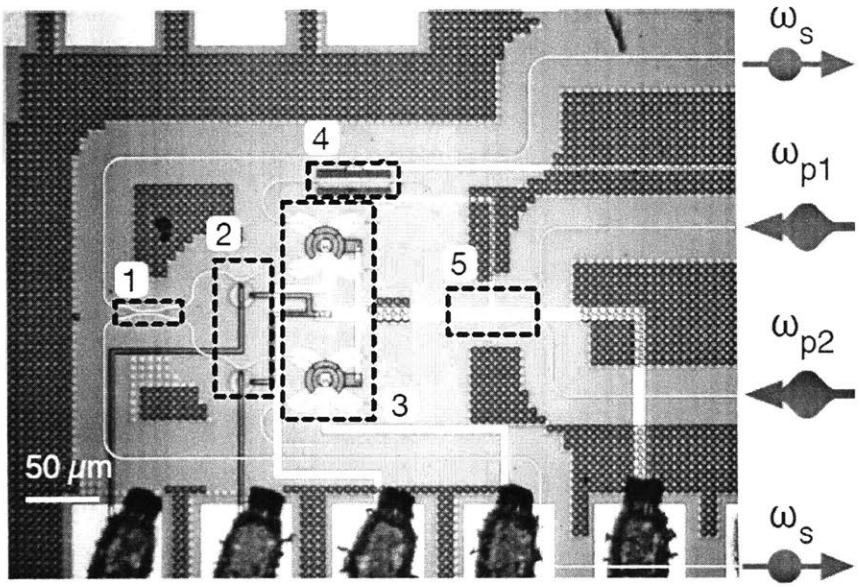

Figure 3.1: Quantum state engineering photonic device. (a) Optical micrograph of the silicon photonic device which incorporates five thermo-optically controlled phase shifters and four microring resonators (two for photon generation and two for pump suppression) in just 0.08 mm^2. Marked components represent the five stages required for quantum state engineering: (1) Pump mixing on a directional coupler, (2) photon generation in two resonators, (3) partial pump suppression in two further resonators, (4) differential phase shift and (5) final directional coupler for quantum interference. From [49].

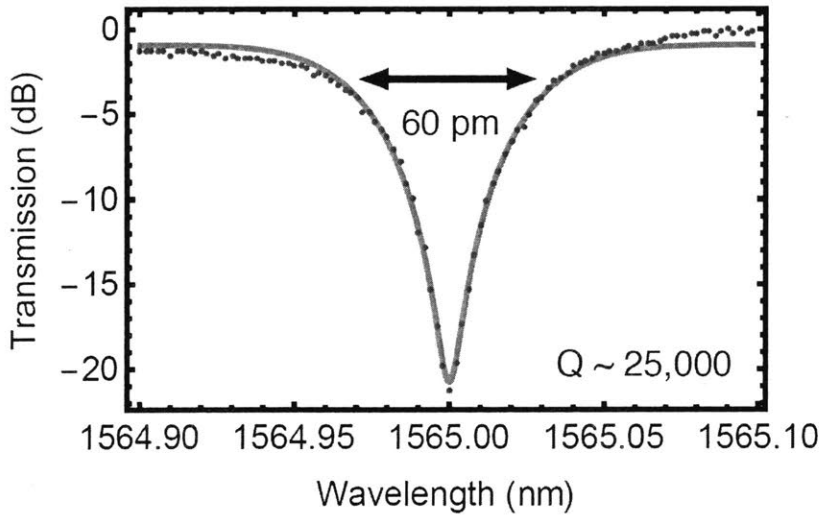

Figure 3.2: Spectrograph of generation rings aligned to 1565 nm along with expected fit. From [49].

nm. These demultiplexing rings serve to filter out the pump laser light, while routing the single photons (generated in the rings upstream) via the drop ports onward to the phase shifter and directional coupler for quantum state engineering. The quantum state of the system at this point is given by:

$$|\psi\rangle = \frac{(|20\rangle_{1,2} + |02\rangle_{1,2})}{\sqrt{2}}. \tag{3.1}$$

where $|n\rangle_m$ represents n photons in the m^{th} optical mode. Next, an integrated doped-silicon thermo-optic phase shifter on one of the bus waveguides conveying the generated photons from the demultiplexing rings is used to apply a differential phase shift to the state, resulting in the following the biphoton N00N state:

$$|\psi\rangle = \frac{(|20\rangle_{1,2} + e^{2i\phi}|02\rangle_{1,2})}{\sqrt{2}}. \tag{3.2}$$

Finally, the state passes through a 50-50 directional coupler to yield the final path-entangled output state via the reverse Hong-Ou-Mandel effect (see Chapter 2):

$$|\psi\rangle_{\text{out}} = \cos\phi(|20\rangle - |02\rangle)/\sqrt{2} + \sin\phi\,|11\rangle\,. \tag{3.3}$$

Setting the differential phase ϕ (controlled by the thermo-optic phase shifter) to 0 only yields output states with both photons in the same output mode (the same arm of the directional coupler), while setting it to $\frac{\pi}{2}$ only yields output states with one photon in each mode.

Operating in a low pump power regime ensures that only one photon pair is likely to be generated in each ring. The resonances of the four rings can be thermo-optically controlled by applying voltages to each ring's embedded resistive heater, which is formed by doped silicon in contact with the metal interconnect layer. To minimize free carrier absorption-induced losses. a low concentration of dopants is used in the region of the waveguide that overlaps with the optical mode. The generation and demultiplexing ring combination leads to a pump suppression of 37 dB, significantly reducing the probability of additional incoherent photon generation in

the bus waveguides, while still maintaining a pump power level that can be detected by photodiodes off-chip. Light is coupled into and out of the chip by custom-built silicon nitride interposers to match the pitch of the silicon waveguides and reduce the mode field diameter to match the tapered on-chip mode converter. The estimated loss per chip facet is -2.5 ± 0.5 dB.

3.2 Experimental configuration

3.2.1 Thermal and electrical control

Thermal stability is of paramount importance in ensuring reliable operation of our device. To this end, the silicon photonic chip is attached with thermal epoxy to a copper mount. A Peltier thermoelectric cooler module and a thermistor are attached to the bottom of the copper mount along with a heat sink, as shown from the side in Fig. 3.3. The entire unit is mounted in an aluminum chassis, and wirebonded (Fig. 3.5) to a PCB to control the on-chip thermo-optic phase shifters (Fig. 3.4).

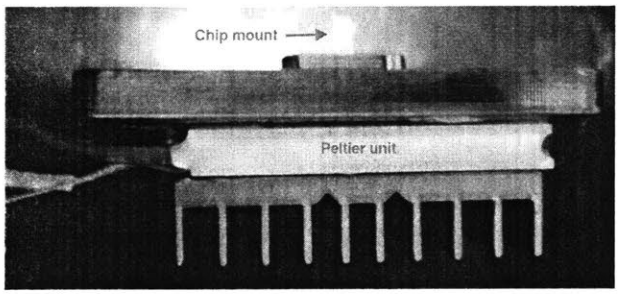

Figure 3.3: Copper mount for chip, with attached Peltier unit and heat sink.

The thermoelectric cooler and thermistor are then connected to a temperature controller that is capable of 0.01°C precision. The PCB is driven by a multichannel custom-built digital to analog converter (DAC) providing 16-bit voltage precision. Python code is used to interface with the temperature controller and DAC, enabling automated control.

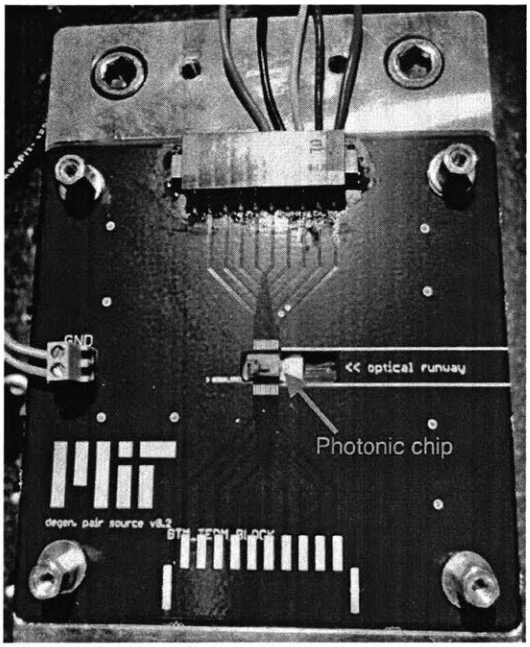

Figure 3.4: Photonic chip and PCB assembly.

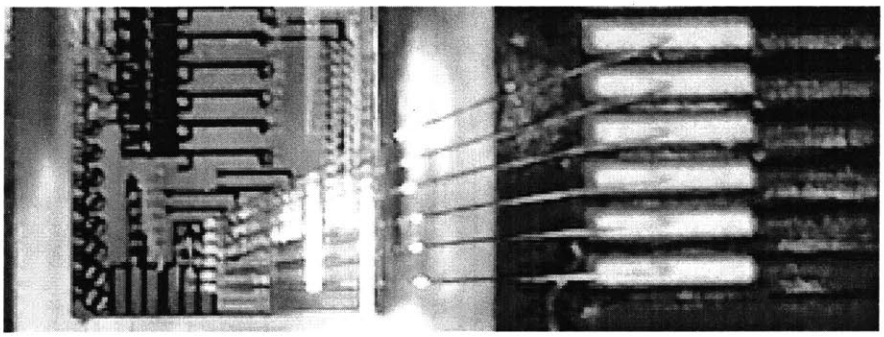

Figure 3.5: Close-up of chip to PCB wirebonds.

3.2.2 Light input and output

A schematic of the experimental setup is shown in Fig. 3.6.

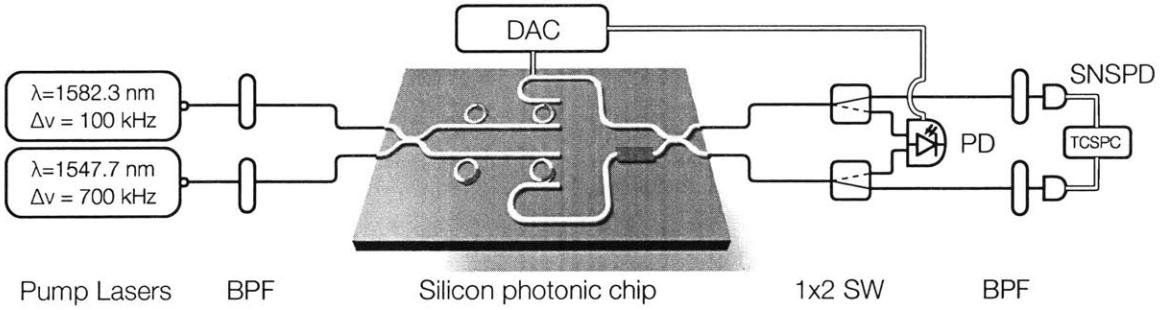

Figure 3.6: Experimental setup. Solid lines refer to fiber optic components and double lines to electrical connections. Two tunable lasers are passed through a bandpass filter (BPF) which then pump the silicon photonic chip. The output passes through a 1×2 switch (SW) which connects either to photodiode array (PD) or superconducting nanowire single photon detectors (SNSPD) and time-correlated single photon counting (TCSPC) module. On-chip thermo-optic phase shifters are controlled by a multi-channel digital-to-analog converter (DAC). From [49].

Two tunable telecom continuous wave lasers are used as the pump signals in this experiment. To produce degenerate signal and idler photons at the central resonance $\lambda_{s,i} = 1565.0$ nm of the tuned generation rings, the first pump is set to wavelength $\lambda_{p_1} = 1582.3$ nm, and the second pump to wavelength $\lambda_{p_2} = 1547.7$ nm, corresponding to $+2$ and -2 FSR away from the central resonance of the generation rings. The pump lasers have sideband suppression of ~70 dB and ~40 dB respectively. The $\lambda_{p_1} = 1582.3$ nm pump is passed through a fiber-coupled tunable bandpass filter providing ~30 dB sideband suppression and the $\lambda_{p_2} = 1547.7$ nm pump is passed through a bulk-optic bandpass filter providing ~70 dB sideband suppression, leading to a total of ~100 dB sideband suppression for each pump. An ultra-high NA fiber array is used to couple the filtered pump light into the input and output directional couplers on the chip.

At the chip output, we have two configurations for off-chip free-space routing of the out-coupled light from both arms of the directional coupler. The collection path of the light depends on whether pump monitoring or single photon counting is taking

place. One path routes the light from both arms of the directional coupler directly to a photodiode array for classical power monitoring, while the other routes the light through two narrow-linewidth bulk-optic bandpass filters in series (for background reduction) to superconducting nanowire single photon detectors (SNSPDs) for photon counting. The path switching is effected by the insertion of bulk-optic flip mirrors in the path of the light. The bulk-optic components are positioned in fiber-coupled U-benches, as shown in Fig. 3.7. The SNSPDs have quantum efficiency of $\sim$ 75% and jitter (timing resolution) of 0.2 ns. The photon signals are time-tagged with a time-correlated single photon counting module.

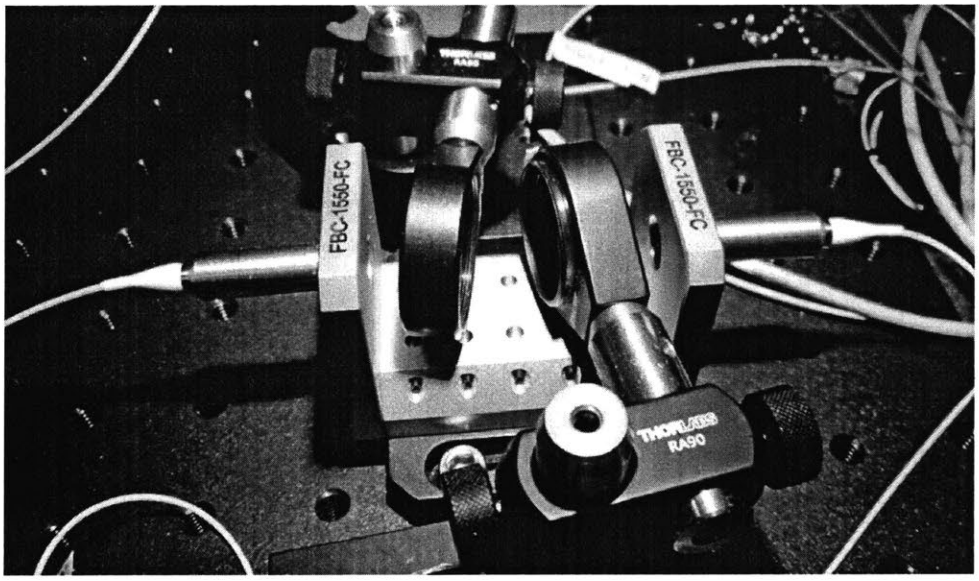

Figure 3.7: Bulk optic output filters in fiber-coupled U-bench.

3.3 Microring resonator stabilization

Control techniques at the device level usually involve a qubit measurement, estimation of a fidelity metric, and feedback onto the control parameters to minimize the infidelity [19, 20]. The robustness of the fidelity estimator is crucial to the success of the control technique [21]. In our experiment, we use the pump laser set to the photon generation wavelength of 1565.0 nm to and detect the total transmitted power at the chip output

with the photodiode, and use it as a metric of the microring resonator alignment. The detected power is at a minimum when the central resonance frequencies of the resonators are precisely aligned to the desired photon generation wavelength, and increases when the central resonance frequencies shifts due to alignment errors. Once the power is detected, an electrical signal is fed back onto the resonators' embedded phase shifters in a closed-loop manner to minimize the transmitted pump power by re-aligning the central resonance. Compared with direct photon detection, the classical probe signal gives an intrinsically higher signal-to-noise ratio.

The power minimization can be implemented via either hardware or software. Here, we use a computational optimization method, as described in the following section. We address two types of errors in the resonance of the microring resonators: static errors and dynamic errors. Static errors arise due to fabrication variations in the resonators such as surface roughness [28], while dynamic errors arise due to thermal variations, electrical noise, crosstalk between devices, etc., leading to fluctuations in the resonators' refractive indices over time and shifting their central resonance. While in principle full knowledge of all parameter dependencies and accurate pre-characterization of voltage-wavelength tuning curves could be used to correct for errors in the resonance frequency of the rings, in reality the process is complicated by thermal crosstalk and electrical noise and requires an *in situ* approach.

3.3.1 Nelder-Mead optimization

Since finding the exact analytical expressions for the net transmitted power of the two rings is infeasible, we use the Nelder-Mead method (also known as the downhill simplex method) [29] to minimize our objective function $T(V_1, V_2)$, the sum of the transmitted powers from the chip's two output channels, over the search space of ordered tuples $[V_1, V_2]$ corresponding to the voltages applied to the phase shifters of the respective generation ring resonators. The Nelder-Mead method is a gradient-free heuristic that was empirically determined to be converge quickly and be robust in the presence of noise.

The steps of the iterative algorithm are qualitatively as follows:

1. Start with an initial simplex with three vertices consisting of an initial guess for $[V_1, V_2]$ and the two points $[V_1 + \Delta, V_2]$ and $[V_1, V_2 + \Delta]$ where Δ is a predetermined step parameter. Evaluate $T(V_1, V_2)$, i.e. measure the total transmitted power, at each of these voltage pair vertices, and order the points in ascending order of their objective function value, from best (lowest objective function value) to worst (highest objective function value):

   $T(\text{Point 1}) < T(\text{Point 2}) < T(\text{Point 3})$.

   If the sample standard deviation of the function values is below a certain predetermined threshold, the convergence condition has been satisfied and the best point is returned as the optimum.

2. Find the midpoint (Point M) of the two vertices besides the worst one. Reflect the worst vertex across the opposite edge along the line joining Point M to the worst vertex to get the new Point R.

   If the new reflected point (Point R) is better than the second best one (Point 2) but worse than the best one (Point 1), make a new simplex with vertices Point 1, Point 2, and the reflected point and start from step 1 with this as the initial simplex.

3. If the new reflected point (Point R) is better than the best one (Point 1), choose an "expanded" Point E further away than Point R along the line from Point M to Point R.

   If Point E is better than Point R, make a new simplex with vertices Point 1, Point 2, and Point E and go to step 1.

   Else make a new simplex with vertices Point 1, Point 2, and Point R and go to step 1.

4. If the new reflected point (Point R) is worse than the best point (Point 1) and the second best point (Point 2) but better than the worst point (Point 3), choose

a "contracted" Point C along the line joining Point M to Point 3. If Point C is better than Point 3, make a new simplex with Point 1, Point 2 and Point C as vertices and go to step 1.

5. Make a new simplex with vertices Point 1, one new point that is between Point 1 and Point 2 on the line joining Point 1 and Point 2, and one new point that is between Point 1 and Point 3 and the line joining Point 1 and Point 3. Go to step 1.

3.3.2 Mathematical coupled rings model

In general, the choice of the initial simplex is very important as a starting simplex that is too small can lead to a local search and converge to a local minimum, failing to find the global minimum. However, in the case of this problem, it can be shown that there is one and only one minimum, so if the Nelder-Mead algorithm converges, it is guaranteed to have found the globally optimal voltage combination. The transmission function of a single ring can be taken to be a Lorentzian:

$$T(\lambda) = \frac{-0.5\Gamma}{(\lambda - \lambda_{las})^2 + (0.5\Gamma)^2} \tag{3.4}$$

where Γ and λ_{las} are the width parameter and laser wavelength respectively. The dependence of the rings' central wavelengths (λ_1 and λ_2) on ring voltages can be modelled as

$$\lambda_1 = \lambda_{01} + \gamma_1 V_1^2 + \alpha_{12} V_2^2 \tag{3.5}$$

$$\lambda_2 = \lambda_{02} + \gamma_2 V_2^2 + \alpha_{12} V_1^2 \tag{3.6}$$

where λ_{01} and λ_{02} are the central resonances of the rings with no applied voltage tuning, coefficients γ_1 and γ_2 correspond to the strength of the rings' wavelength dependence on voltage applied to themselves, and the coefficient α_{12} corresponds to the strength of the each ring's wavelength dependence on voltage applied to the

other. The voltage-squared dependence of the central wavelength on voltage arises from linearity of the wavelength shift with temperature, and hence with the dissipated power. In a physically realistic case, both the ratios $\frac{\gamma_1}{\alpha_{12}}$ and $\frac{\gamma_2}{\alpha_{12}}$ will be much greater than both $\frac{\lambda_{las}-\lambda_{01}}{\lambda_{las}-\lambda_{02}}$ and $\frac{\lambda_{las}-\lambda_{02}}{\lambda_{las}-\lambda_{01}}$. The total transmission of two rings in series is given as:

$$T(\lambda_1, \lambda_2) = \frac{-0.5\Gamma}{(\lambda_1 - \lambda_{las})^2 + (0.5\Gamma)^2} * \frac{-0.5\Gamma}{(\lambda_2 - \lambda_{las})^2 + (0.5\Gamma)^2} \tag{3.7}$$

and the total transmission in parallel as:

$$T(\lambda_1, \lambda_2) = \frac{-0.5\Gamma}{(\lambda_1 - \lambda_{las})^2 + (0.5\Gamma)^2} + \frac{-0.5\Gamma}{(\lambda_2 - \lambda_{las})^2 + (0.5\Gamma)^2}. \tag{3.8}$$

Both the series and parallel transmission functions have critical points where the conditions $\frac{\partial T}{\partial \lambda_1} = 0$ and $\frac{\partial T}{\partial \lambda_2} = 0$ hold. In order to satisfy both conditions, we require $V_1 = 0$ or $\lambda_1 = \lambda_{01} + \gamma_1 V_1^2 + \alpha_{12} V_2^2 = \lambda_{las}$, and $V_2 = 0$ or $\lambda_1 = \lambda_{01} + \gamma_1 V_1^2 + \alpha_{12} V_2^2 = \lambda_{las}$. Out of the four possible combinations, only one gives a minimum (the others are a maximum and saddle points):

$$\lambda_1 = \lambda_{01} + \gamma_1 V_1^2 + \alpha_{12} V_2^2 = \lambda_{las} \tag{3.9}$$

$$\lambda_2 = \lambda_{02} + \gamma_2 V_2^2 + \alpha_{12} V_1^2 = \lambda_{las} \tag{3.10}$$

Given the physically realistic stipulations on γ_1, γ_2, α_{12}, $\lambda_{las} - \lambda_{01}$ and $\lambda_{las} - \lambda_{02}$, the two equations above are guaranteed to have a solution with non-zero values of V_1 and V_2, which corresponds to tuning both rings to the laser wavelength. Hence, there is only one global minimum value of the transmission function for non-negative voltages, and no local minima. This guarantees that if our search converges, it will have converged to the true global minimum. This model may be generalized to an arbitrary number of ring resonators in series or parallel, such that the total transmission of N rings in series will be given by

$$T(\lambda_1, \lambda_2, \cdots, \lambda_N) = \prod_{i=1}^{N} \frac{-0.5\Gamma}{(\lambda_i - \lambda_{las})^2 + (0.5\Gamma)^2} \tag{3.11}$$

and the total transmission in parallel by

$$T(\lambda_1, \lambda_2, \cdots, \lambda_N) = \sum_{i=1}^{N} \frac{-0.5\Gamma}{(\lambda_i - \lambda_{las})^2 + (0.5\Gamma)^2} \tag{3.12}$$

As in the two-ring case above, the sole minimum of the transmission function is achieved when all rings are individually tuned to the laser wavelength, and there are no local minima.

3.3.3 Static error correction

We run the feedback-controlled correction protocol 100 times. For the static error correction test. In each run, the pump laser is set to the desired generation wavelength and initial voltages for the two generation rings are chosen at random from normal distributions centered on 3.60 V and 3.56 V (independently determined to be near optimal from prior characterization) respectively with a standard deviation of 0.2 V. An iterative Nelder-Mead optimization algorithm is used to arrive at the generation ring voltage combination that minimizes the sum of the optical output powers of the microring resonators as measured by the off-chip photodiode array.

Out of the 100 attempted runs 62 succeed, requiring an average of 57 iterations to converge, as shown in Fig. 3.8. The voltage of each generation microring resonator is tracked during optimization. The final voltage of each ring differs by 40 mV, demonstrating the variability in fabrication of the devices and the importance of static error correction. Additionally, by repeatedly running this protocol over a period of 7 hours, we observe a total reduction in the voltages by 18 mV, which can likely be ascribed to a systematic drift in laboratory temperature.

3.3.4 Dynamic error correction

We simulate and correct for two classes of dynamic error typically seen in photonic quantum systems: (1) environmental temperature fluctuations and (2) crosstalk between thermo-optic phase shifters. Temperature fluctuations are induced by varying

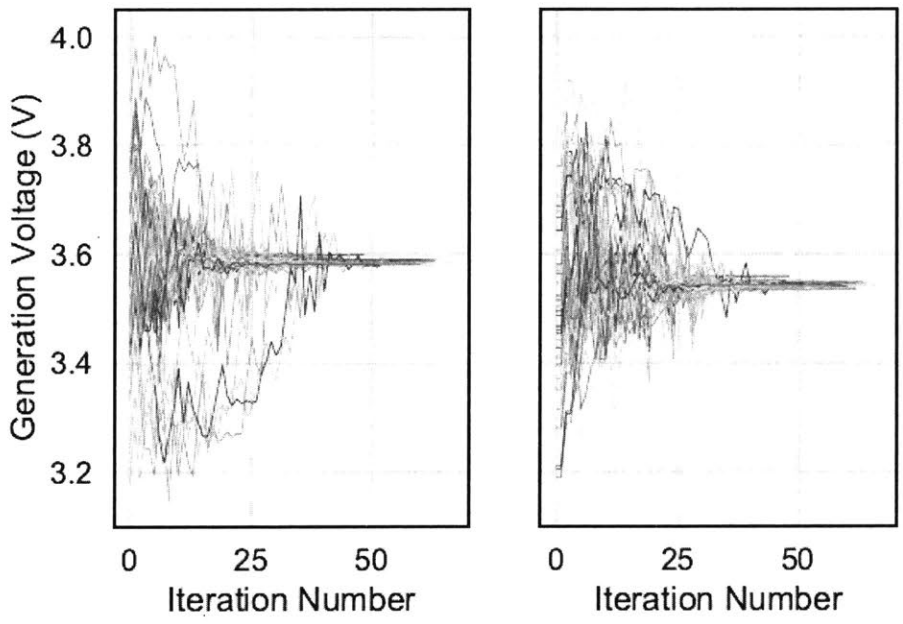

Figure 3.8: Static error correction. The change in voltages for each generation ring resonator during 62 alignment protocols. Solution voltages not only vary between resonators (a static offset due to fabrication variations) but also over the course of the experiment due to a systematic change in laboratory conditions. A version of this figure appears in [49].

the chip temperature through an auxiliary Peltier control system onto which the device is mounted. We program a random walk in temperature in increments and decrements of 0.1°C over the course of one hour for a net increase of 1°C. The inset in Fig. 3.9 (top left) shows one such instance of a random walk. After each increment or decrement, the correction protocol is run to re-align the resonances. Fig. 3.9 (top row) plots spectrographs for this instance which show the shift in the central resonance of the microring resonators as a result of this temperature variation in the absence of dynamic frequency stabilization (left) and in the presence of our *in situ* correction approach (right).

The implementation of our correction protocol results in a standard deviation in the central resonance wavelength of only 0.56 pm ($9.4 \times 10^{-3}\Delta\lambda$, where $\Delta\lambda$ is the cavity linewidth), whereas in the absence of any correction protocol, a total variation of 84.0 pm ($1.4\Delta\lambda$) is observed. This corresponds to a 150-fold increase in resonance stability.

Similarly, we induce thermal crosstalk by incrementally increasing the phase shifter voltage from 0 to 6.5 V. Fig. 3.9 (bottom row) shows the resulting central wavelength shift when no correction is implemented (left) and when the *in situ* correction protocol is implemented (right). Dynamic frequency stabilization yields a stability of 0.65 pm ($1.1 \times 10^{-2}\Delta\lambda$), a 70-fold improvement compared with a total variation of 45 pm ($0.75\Delta\lambda$) in the uncorrected case.

3.3.5 Tuning curves

To compare the performance of our *in situ* correction technique with the results obtained using pre-determined models, we independently characterize the temperature vs generation ring voltage relations and the phase shifter voltage versus generation ring voltage relations of the resonators over the same range of temperatures and phase shifter voltages as in the temperature random walk and phase shifter voltage sweep described above. By sweeping the temperature, T, from 30 to 31 degrees and iteratively aligning the rings at each voltage using the Nelder-Mead algorithm, we obtain

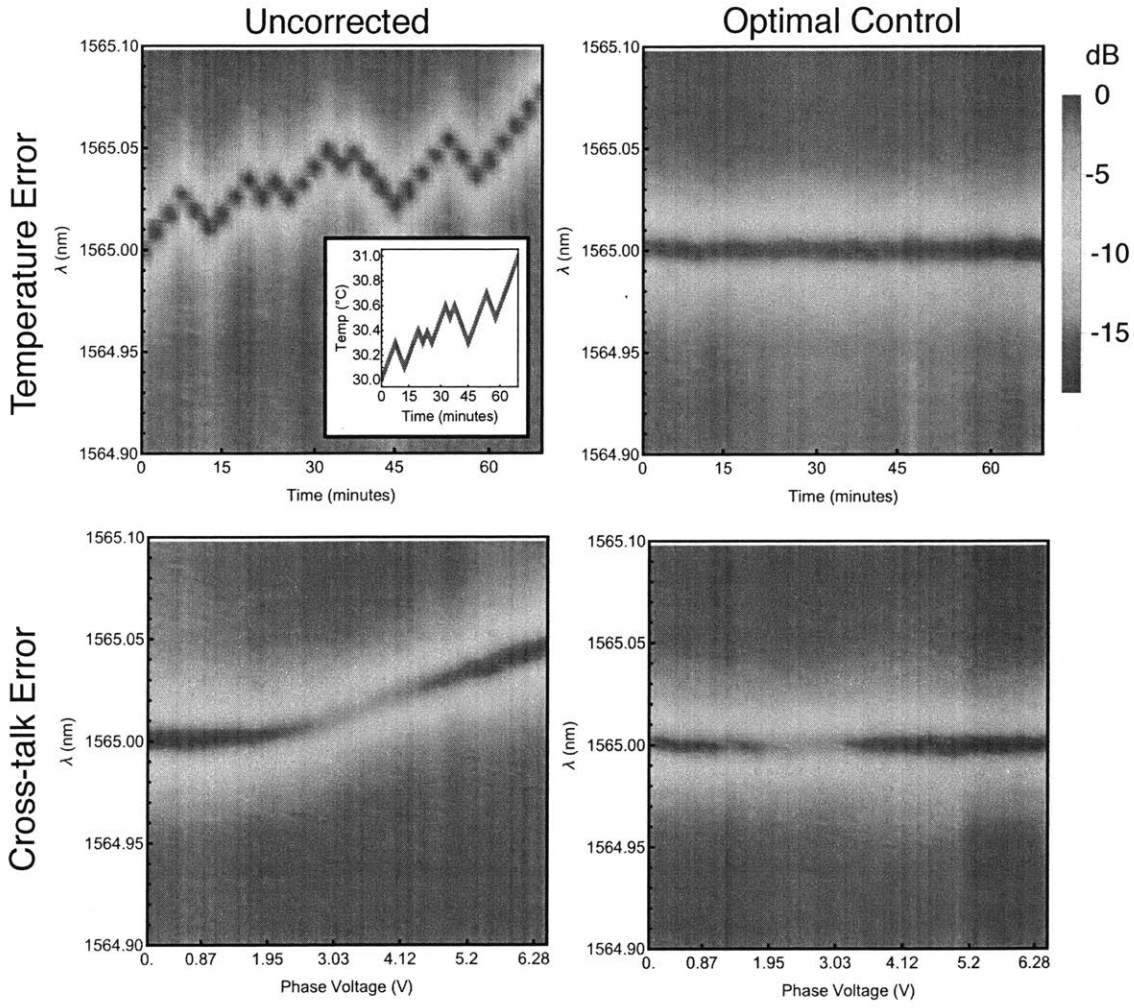

Figure 3.9: Dynamic error correction. Spectrographs are taken by tuning an auxiliary laser and measuring the output power on a photodiode. The left column shows spectrographs of the resonators as the chip temperature is varied according to the random walk in the inset. The right column shows spectrographs of the resonators as a voltage is applied to an adjacent thermo-optic phase-shifter. Thermal cross-talk causes the resonance of the resonators to shift, which should otherwise remain untouched by the phase shifter. In each instance the dynamic stabilization gives a two orders of magnitude increase in the resonance stability. A version of this figure appears in [49].

generation ring voltage (V_1 and V_2) versus temperature data (Fig. 3.10). Based on five such sweeps, we obtain the following best-fit linear tuning curve for the dependence of the ring voltages on temperature:

$$V_1(T) = -0.06090T + 5.568 \tag{3.13}$$

$$V_2(T) = -0.06166T + 5.546 \tag{3.14}$$

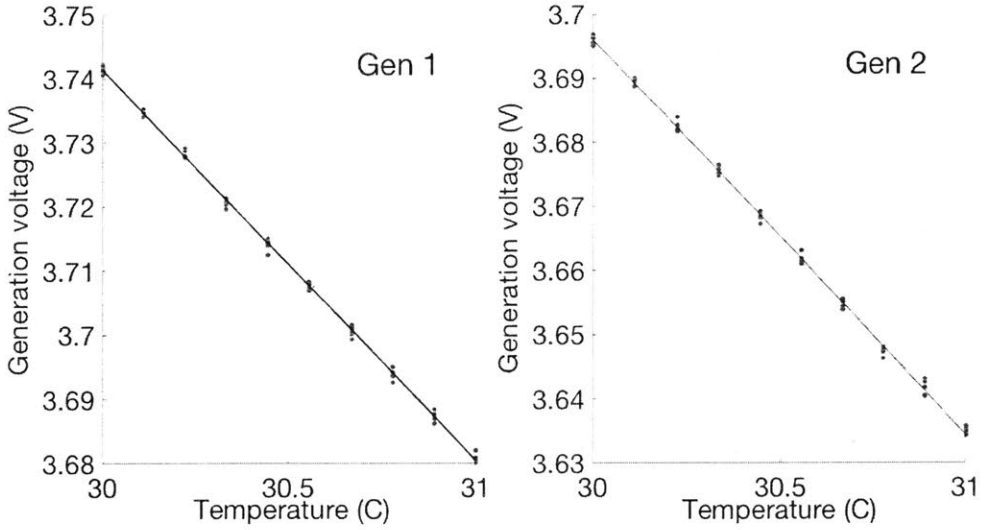

Figure 3.10: Temperature tuning curve derived from five sets of data. From [49].

Similarly, by sweeping the phase shifter voltage, V_p, from 0 to 6.5 volts and aligning the rings at each voltage using the Nelder-Mead algorithm, we obtain ring voltage versus phase shifter voltage data (Fig. 3.11). Based on five sweeps, we obtain a best-fit quadratic tuning curve for the dependence of the ring voltages on the phase shifter voltage:

$$V_1(V_p) = -0.0007192V_p^2 - 0.0003439V_p + 3.746 \tag{3.15}$$

$$V_2(V_p) = -0.0008414V_p^2 - 0.000576V_p + 3.702 \tag{3.16}$$

To evaluate the performance of tuning curve-based resonance correction in comparison with feedback control-based correction, we run the same temperature random

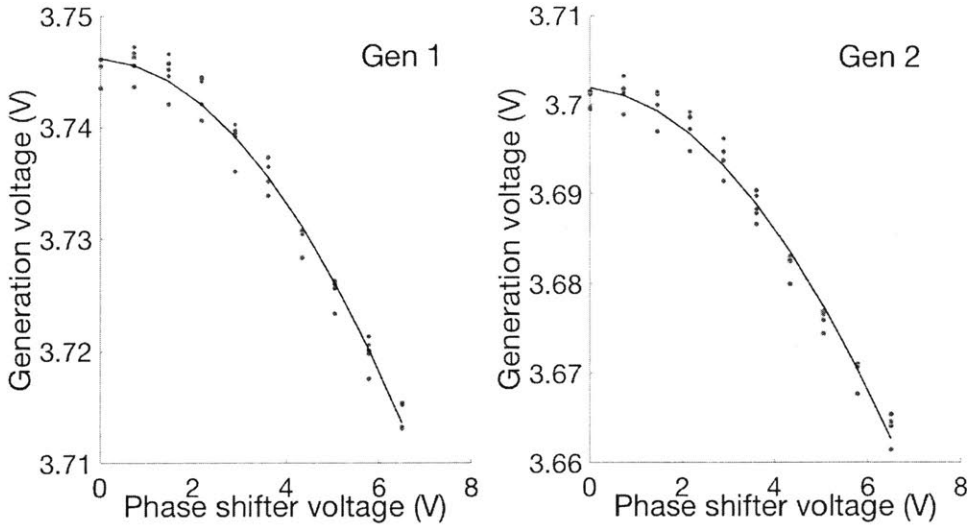

Figure 3.11: Voltage tuning curve from five sets of data. From [49].

walk and phase shifter voltage sweep as above. After each temperature or phase shifter voltage adjustment, the generation ring voltages are set to the values according to the pre-determined functions instead of being iteratively optimized on the fly. It is observed that while alignment using pre-determined tuning curves leads to 15-fold and 5-fold improvements over the correction-less case for the temperature and voltage errors respectively, our iterative alignment protocol still outperforms the tuning curve-based correction by an order of magnitude in both instances. Moreover, our feedback-based technique can naturally be applied to dynamic corrections where the noise model is unknown.

3.4 Feedback-controlled quantum state engineering

To demonstrate that our *in situ* approach can be performed in parallel to the quantum computation, we apply our feedback protocol to the task of quantum state engineering. The phase shifter voltage is incrementally swept from 0V to 6.5V. At each voltage increment, the chip output is routed first to the photodiode so that the feedback con-

trol protocol can be applied to align the generation ring resonances. Subsequently the output collection path is switched to the superconducting nanowire single photon detectors for coincidence counting. As seen from Equation 3.3, a linear variation in the differential phase ϕ causes a sinusoidal change in the probability amplitude of the $|11\rangle$ state, and a sine-squared change in the coincidence probability:

$$P(|11\rangle) = \sin^2(\phi) \tag{3.17}$$

Without the frequency control step (Fig. 3.12(a), red), thermal cross-talk from the differential phase decouples the microring resonators and produces an asymmetry in the interference fringe. To quantify this asymmetry, we introduce the contrast metric $C_{\text{asy}} = |C_1 - C_2|/\max(C_1, C_2)$ as the normalized difference between the coincidence counts C_1 at $\phi = \pi/2$ and counts C_2 at $\phi = 3\pi/2$, where $C_{\text{asy}} = 0$ in the ideal case. From the coincidence data, it is observed that in the absence of correction, $C_{\text{asy}} = 0.791$. Applying the frequency control protocol is found to recover the symmetry of the interference fringe and yield a contrast $C_{\text{asy}} = 5.61 \times 10^{-3}$. The quantum visibility, given by $V_{\text{q}} = (C_{\text{max}} - C_{\text{min}})/C_{\text{max}}$ where $C_{\text{max}}(C_{\text{min}})$ is the maximum (minimum) measured coincidence counts, quantifies the indistinguishability of the photons . Once the interference fringe is fitted (Fig. 3.12(a), blue line) to account for the nonlinear phase-voltage relation of the thermo-optic phase shifter [25], the quantum visibility is extracted to be $V_{\text{q}} = 0.938 \pm 0.021$.

The deviation from unity visibility can be primarily attributed to higher order photon events, which result from the high pump power required to achieve a reasonable signal-to-noise ratio in the presence of lossy off-chip filters. In future, the monolithic integration of lasers [30], single photon detectors [7] and filters [5, 31] may significantly reduce optical power constraints.

Finally, we measure the coincidence count rate as a function of the input pump power; the results are shown in Fig. 3.13, with $\phi = \pi/2$ for maximum coincidence probability. At each optical power setting the frequency stabilization protocol to account is applied for the refractive index changes in the microring resonators arising

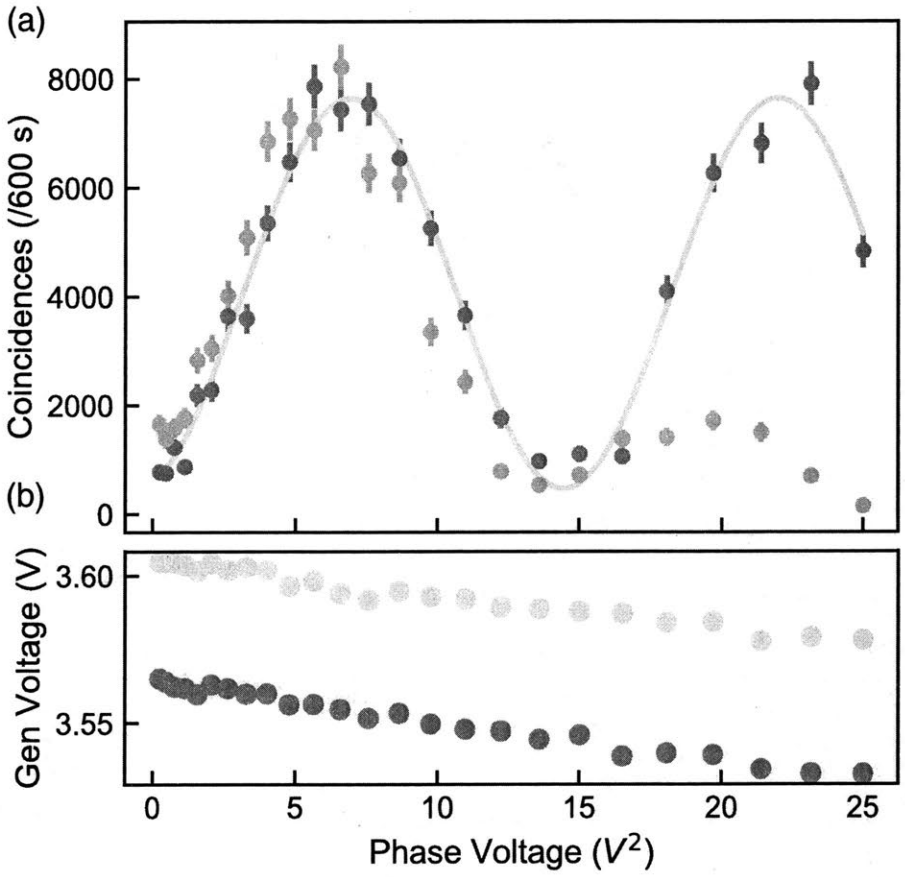

Figure 3.12: Error-corrected quantum state engineering. (a) Coincidence count rate plotted as a function of the square of the differential phase voltage, with (blue) and without (red) frequency stabilization, alongside a sinusoidal fit (light blue). Coincidences have been normalized for detector channel inefficiencies and error bars assume Poissonian counting statistics. The symmetry in the locked fringe can clearly be observed in comparison to the unlocked. (b) Variation in microring resonator control voltages over the course of the differential phase sweep when frequency locking is applied. From [49].

from a combination of Kerr, thermal, and free-carrier dispersion effects [32].

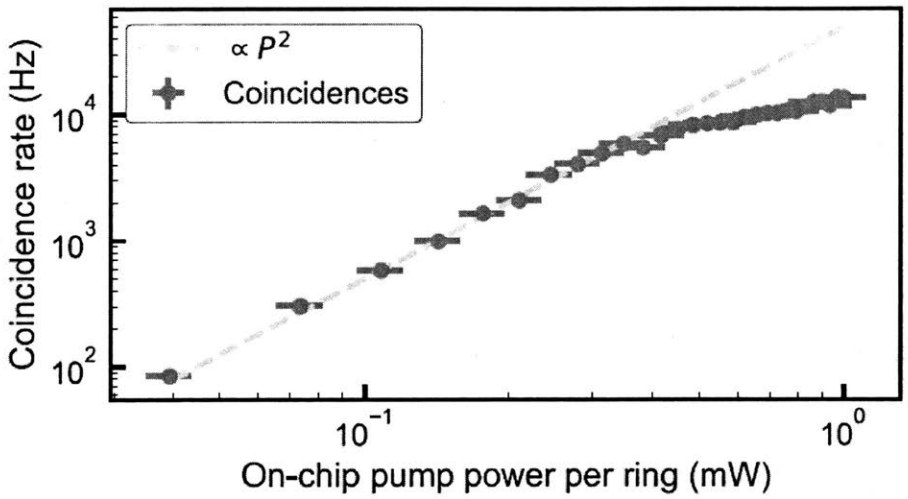

Figure 3.13: Coincidence count rate plotted as a function of input power per ring (blue points) and an expected quadratic dependency based on a purely four-wave mixing process (light blue line). From [49].

We reach an off-chip photon generation rate of 13.5 kHz (corrected for detector channel inefficiencies). The rate is primarily limited by two photon absorption; this can be seen in Fig. 3.13, where the measured coincidence count rate is plotted against the expected quadratic dependence (Fig. 3.13, blue dashed), showing deviations at powers greater than 200 μW. Progress on mid-IR silicon photonics might help to overcome this limitation, since two photon absorption becomes negligible at wavelengths longer than 2.2 μm [33, 34].

Chapter 4

Towards four-photon interference with unentangled photon pairs

In order to achieve high-visibility quantum interference, photons in each generated pair must be unentangled and yield high-purity states. To minimize correlations between the signal and idler photon in a pair, a broad pump spectrum must be used, and the resonance quality factor of the pump must be significantly smaller than the signal and idler resonances. It must be possible to tune the pump quality factor independently of the signal/idler quality factors, which is not feasible with conventional ring resonators. Instead, an interferometric coupling ring with two coupling points (essentially a Mach-Zehnder interferometer) as in Fig. 4.1 can be used to overcome the problem of undesirable correlations between photons in a generated pair.

4.1 Four-photon generation device

Fig. 4.2 shows the photonic chip used in this in-progress experiment. This chip contains four conventional Mach-Zehnder interferometers, one interferometric photon generation ring, four demultiplexing ring resonators, and thermo-optic phase shifters (resistive heaters) on each device.

Photons are generated by non-degenerate spontaneous four wave mixing in this

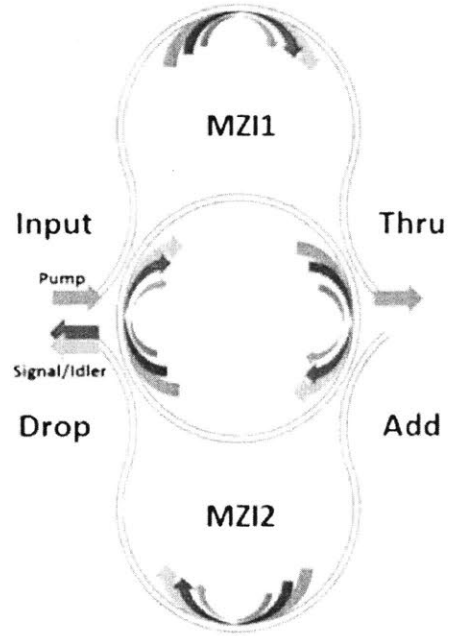

Figure 4.1: Interferometrically-coupled photon generation device, enabling independent control of pump, signal and idler resonances. Adapted from [15].

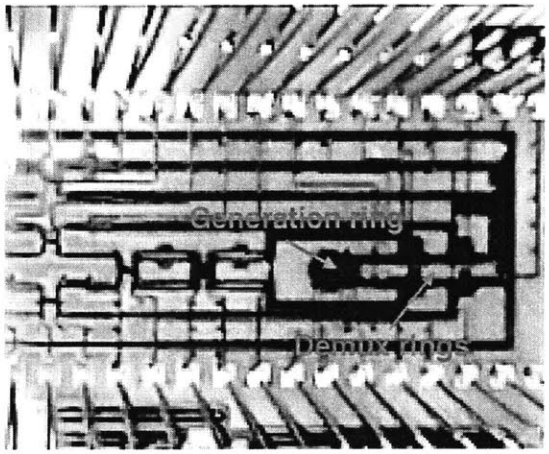

Figure 4.2: Quantum photonic chip for four-photon generation, including an interferometrically-coupled photon generation ring and four demultiplexing rings.

experiment, with a pump at a single frequency generating photons at two different frequencies. Pump light is input through the topmost Mach-Zehnder interferometer to the large central generation ring. The interference between the light in the generation ring and the light in the bus waveguide can be tuned with two integrated resistive heaters, allowing for individual control such that the pump mode couples at one point and the signal/idler modes at the other. Four photons–two signals and two idlers–are generated in the large central ring, and pair-wise separated into the four output channels by the demultiplexing rings. Fig. 4.3 shows a schematic of the photon generation and on-chip routing, where ω_p is the pump frequency, ω_s the signal frequency, and ω_i the idler frequency.

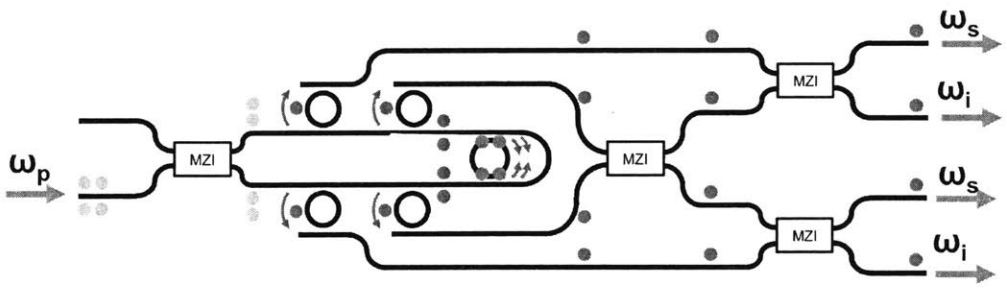

Figure 4.3: Four-photon generation scheme. The yellow dots represent the pump photons, the blue dots the signal photons, and the red dots the idler photons. Adapted from [69].

4.2 Experimental setup

The thermal and electrical control of this chip is implemented identically to the chip in Chapter 3. Fig. 4.4 shows the experimental setup.

A pulsed laser at with repetition rate 60 MHz is set to the pump wavelength of 1563.5 nm (matching a pre-characterized resonance of the generation ring), for photon generation at 1551.2 nm and 1575.9 nm. The pump is passed through band-pass filters for a net 88 dB sideband suppression. Because of the limited availability of superconducting single photon detectors in the lab, the chip outputs are passed

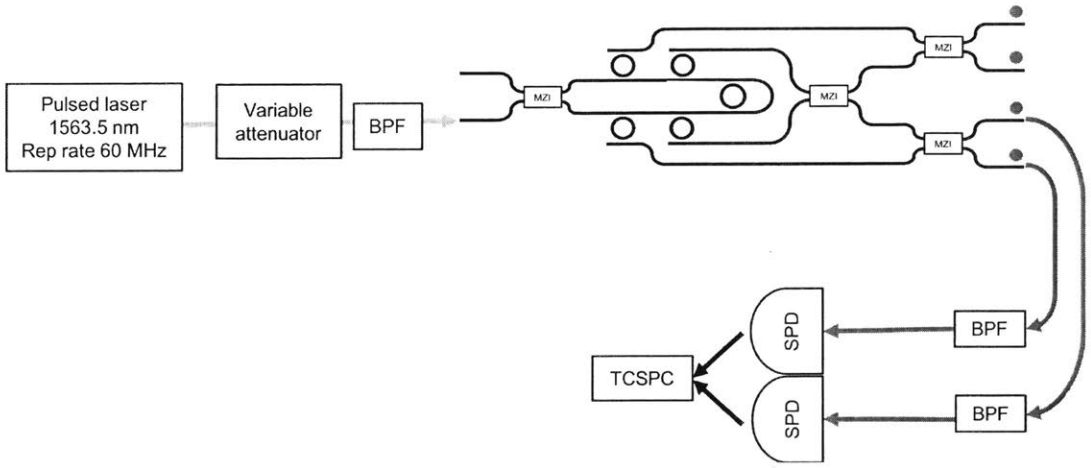

Figure 4.4: Experimental setup for four-photon generation experiment. The pump laser (1563.5 nm) is passed through a variable optical attenuator before bandpass filtering (BPF). The output photons are routed to superconducting nanowire single photon detectors (SPD) and time-tagged using a time-correlated single photon counting (TCSPC) module. Adapted from [69].

through further bandpass filters for pump suppression and routed two at a time to the detectors to observe coincidences. However, due to insufficient pump extinction with the bandpass filters at the output, it has not been possible to observe interference thus far. Improvements to the setup are in progress, including the installation of more bandpass filters in series at the outputs in order to achieve higher pump suppression. The expected result of this experiment is the observation of four-photon heralded Hong-Ou-Mandel interference with very high visibility due to the absence of entanglement and spectral correlations between the generated photons.

Chapter 5

Non-volatile phase shifters based on shape-memory materials

A major challenge in managing the increasing complexity of photonic integrated circuits is to develop scalable and energy-efficient programming and trimming of phase shifters within optical components. For example, to perform an arbitrary unitary linear-optical operation on N input and output modes, the number of required phase shifters scales as $O(N^2)$; this figure can be in the hundreds, making power dissipation a major concern. This leads to the need for non-volatile phase shifters, which, unlike the approaches described in Section 2.1.3, would not require a constant supply of power to remain in the "on" state. Additionally, for fully-integrated on-chip quantum computing at cryogenic temperatures around 4K (necessary for integration of superconducting single photon detectors and solid-state atom-like emitters), phase shifters must be able to operate with low loss at such low temperatures [8]. Phase-change materials, such as chalcogenides, have emerged as promising candidates for non-volatile phase shifters [64]; however, these materials traditionally introduce residual absorption and higher losses by evanescently coupling to the waveguide fields.

Here, we introduce a new concept for phase modulation based on the photoelastic effect in silicon, controlled via strain through nonvolatile actuators. In addition, we consider the possibility of using the same shape-memory materials to produce a

strain-induced electro-optic effect in silicon. In particular, to strain SOI waveguides, we propose the integration of shape-memory ceramics and alloys, such doped zirconia and nickel titanium alloys, that transduce strain into an optical waveguide while transforming between two different crystalline forms. This non-volatile phase shifter concept is investigated through finite-element simulations based on experimentally measured material properties. We show that the shape-memory effect can potentially produce a relative index shift $\frac{\Delta n_{eff}}{n_{eff}}$ (where $n_{eff} = 2.55$ for our SOI waveguides at 1550 nm) on the order of 10^{-3}.

5.1 Strain-induced phase modulation

The refractive index of a waveguide can be perturbed locally by the application of mechanical stress [56]. The applied stress can serve two purposes: 1) modulating the refractive index via the photoelastic effect, and 2) breaking the centro-symmetry of silicon to induce a second-order nonlinearity ($\chi^{(2)}$) to enable an otherwise non-existent electro-optic effect. Photoelastic effect-induced phase modulation has been successfully demonstrated before, for example in [56], where a silica waveguide in one arm of a Mach-Zehnder interferometer was compressed using a piezo-electric actuator to effect a phase shift, and the characteristic Hong-Ou-Mandel interference observed with heralded single photon inputs. The use of silicon nitride to break the centro-symmetry of silicon with strain and induce an electro-optic effect was first demonstrated in [55], where a ($\chi^{(2)}$) of $\sim$ 15 pm/V was extrapolated. Building upon this technique, [57] demonstrated an integrated electro-optic Mach-Zehnder modulator with an extrapolated $\chi^{(2)}$ of 122 pm/V. However, a non-volatile strain-actuated approach is still outstanding.

5.1.1 Photoelastic effect

The photoelastic effect can be described by the same tensor formalism as the linear electro-optic (Pockels) effect [3]. The photoelastic effect-induced change in refractive

index Δn_i along a specific direction $i \in \{x, y, z\}$ resulting from applied stress is obtained as follows, where n_0 is the unperturbed index, ρ_{ij} the photoelastic tensor element, and ϵ_j the strain along direction j:

$$\Delta\left(\frac{1}{n^2}\right)_i = \sum_{j=1}^{3} \rho_{ij}\epsilon_j \tag{5.1}$$

Since $\Delta\left(\frac{1}{n^2}\right)_i \approx -\frac{2}{n_0^3}\Delta n_i$, we have

$$\Delta n_i \approx -\frac{1}{2} n_0^3 \sum_{j=1}^{3} \rho_{ij}\epsilon_j. \tag{5.2}$$

Assuming a very long waveguide in the z-direction such that the strain in the z-direction is negligible, we consider the effective index change cross a two-dimensional cross section of the waveguide perpendicular to the direction of light propagation. Applying the stress-strain relation for an isotropic medium, the refractive index change is obtained as a function of the applied stresses $\sigma_{i,j,k}$:

$$\Delta n_x = n_x - n_0 = -C_1\sigma_x - C_2(\sigma_y + \sigma_z) \tag{5.3}$$

$$\Delta n_y = n_y - n_0 = -C_1\sigma_y - C_2(\sigma_x + \sigma_z) \tag{5.4}$$

The photoelastic constants C_1 and C_2 are related to the material's Young's modulus (E) and Poisson's ratio (ν) as follows [70]:

$$C_1 = \frac{n^3}{2E}(\rho_{11} - 2\nu p_{12}) \tag{5.5}$$

$$C_2 = \frac{n^3}{2E}(-\nu\rho_{11} + (1-\nu)p_{12}) \tag{5.6}$$

5.1.2 Strain-induced $\chi^{(2)}$

Induced $\chi^{(2)}$-based phase shifters do not meet the criterion of non-volatility, but are considered here as an insightful case study. Although it is theoretically possible to

estimate $\chi^{(2)}$ values for silicon waveguides from ab-initio calculations, discrepancies have been reported between theoretically-derived values and the results from experimental observations, suggesting that there may be some missing physics in current models [62]. For example, a $\chi^{(2)}$ of less than 0.05 pm/V is predicted by most theoretical models, although experiments have yielded values two orders of magnitude higher. To obtain a more accurate estimate of $\chi^{(2)}$, [62] proposes a "figure of merit" approach to infer the induced silicon $\chi^{(2)}$, based on the proportionality of $\chi^{(2)}$ to the strain gradient $\frac{\partial \varepsilon_{xx}}{\partial y}$. The figure of merit is given by the overlap integral of the strain gradient and the normalized mode intensity across the waveguide transverse cross-section, similar to the calculation of the mode effective index:

$$FOM = \frac{\iint_{Si} \frac{\partial \varepsilon_{xx}}{\partial y} |E|^2 dxdy}{\int_{-\infty}^{\infty} \int_{-\infty}^{\infty} |E|^2 dxdy} \tag{5.7}$$

Based on limited data from experimentally observed $\chi^{(2)}$ values, [62] finds a strong linear correlation (R^2=0.8976) between $\chi^{(2)}$ and the calculated FOM from simulations: $\chi^{(2)} = 0.0124 * FOM$. Thus, once the FOM is calculated based on a waveguide simulation, an estimate of $\chi^{(2)}$ can be found.

Following [62], we derive the index shift as a result of $\chi^{(2)}$ and an applied electric field. To first order for non-magnetic media, we have

$$n_0 = \sqrt{1 + \chi^{(1)}} \tag{5.8}$$

More generally, for χ including higher-order terms, we have

$$n = \sqrt{1 + \chi} \tag{5.9}$$

For materials with χ including a non-zero $\chi^{(2)}$ and negligible higher-order nonlinearities, we have

$$n = \sqrt{1 + \chi^{(1)} + 2\chi^{(2)} E} = \sqrt{(1 + \chi^{(1)}) \left(1 + \frac{2\chi^{(2)} E}{1 + \chi^{(1)}}\right)} \tag{5.10}$$

Since

$$\frac{\chi^{(2)}E}{1+\chi^{(1)}} \ll 1,$$

$$n \approx n_0\sqrt{\left(1+\frac{2\chi^{(2)}E}{n_0^2}\right)} \tag{5.11}$$

$$n \approx n_0\left(1+\frac{1}{2}\frac{2\chi^{(2)}E}{n_0^2}\right) \tag{5.12}$$

Using the Taylor expansion for $n(E) = n_0 + \Delta n = n_0 + n'(E)E + ...$, it follows that

$$n_0 + \Delta n \approx n_0\left(1+\frac{\chi^{(2)}E}{n_0^2}\right) \tag{5.13}$$

Finally, we have

$$\Delta n \approx \frac{\chi^{(2)}E}{n_0} \tag{5.14}$$

5.2 Shape-memory phase shifter concept

Shape-memory materials possess the ability to undergo thermally-activated hysteretic transformations between martensitic (low temperature) and austenite (high temperature) forms; upon re-heating/cooling, these materials can recover their original shape [53, 54]. The doping concentrations of shape-memory ceramics and alloys can be engineered to obtain transformation temperatures suitable for operation with silicon photonic integrated circuits. Changes between the martensite and austenite forms may be achieved by momentarily heating or cooling the chip and/or locally heating the shape-memory material with resistive heaters. Unlike in the case of thermo-optic phase shifters, the devices would not need a constant supply of power to remain in a given state, leading to significant decreases in net energy consumption for a large-scale photonic circuit. Based on data from the literature, we simulate a volume expansion of 3% between the two crystalline forms to obtain the stress exerted on the silicon waveguide [68].

5.2.1 Proposed device structure

Two phase shifter geometries that we consider in the SOI architecture are shown below (Fig. 5.1 and Fig. 5.2). We model our phase shifter as a 2μm wide, 500 nm tall region of polycrystalline zirconia adjacent to the partially-etched silicon rib waveguide. Two possible configurations are explored via simulations: one where the waveguide is fully clad in oxide, and another where the oxide is removed both above and below the one partially-etched silicon contact, so that the strain transduction region is undercut. The SOI waveguide has a height of 220 nm and a width of 500 nm, with 2μm wide, 90 nm thick silicon contact regions.

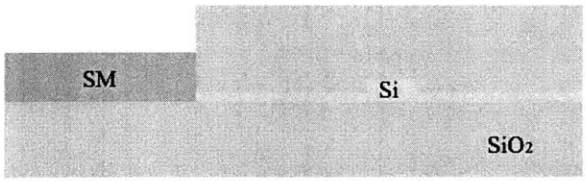

Figure 5.1: Fully oxide-clad waveguide with shape-memory phase shifter.

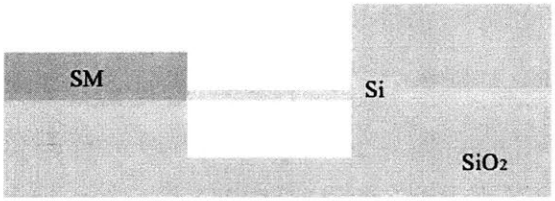

Figure 5.2: Partially oxide-clad waveguide with shape-memory phase shifter.

5.2.2 Simulation results

In our finite element simulations (COMSOL), we model a maximum volume expansion of 3% as shape-memory phase shifter undergoes thermal cycling between martensite and austenite phases. The resulting horizontal boundary stresses for the fully-oxide-clad and undercut structures are on the order of 0.1 GPa and 1 GPa respectively (Fig. 5.3 and Fig. 5.4).

Fig. 5.5 and Fig. 5.6 show the absolute value of the relative effective index change

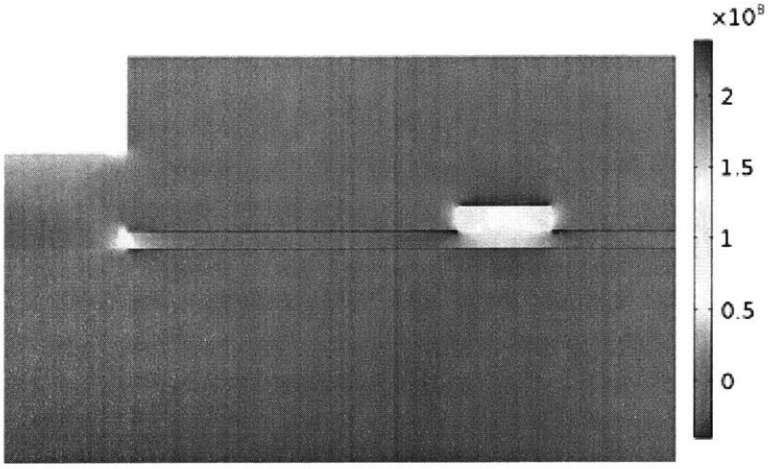

Figure 5.3: Fully oxide-clad waveguide stress profile (axis in Pa).

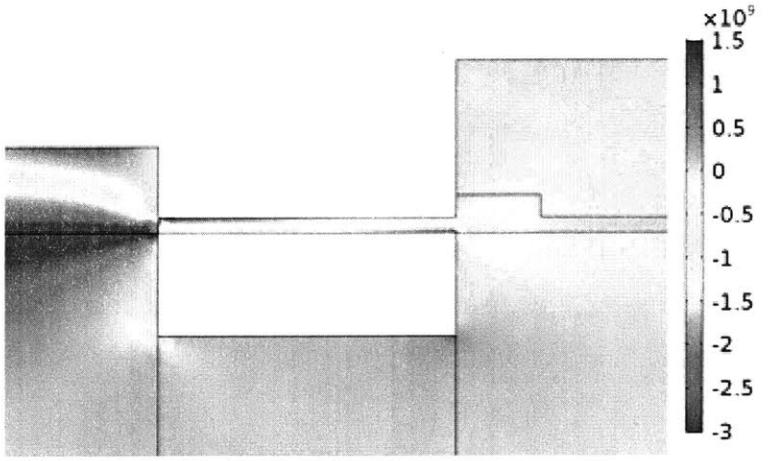

Figure 5.4: Partially oxide-clad waveguide stress profile (axis in Pa).

$\frac{\Delta n_{eff}}{n_{eff}}$ as a function of the volume expansion from 0 to 3%, as obtained from our finite element simulations of the fundamental quasi-TE mode of the waveguide.

The partially-clad structure gives a greater effective index shift, as well as a strong linear correlation (R2 = 0.9999) between volume expansion and index change. This is likely due to the absence of competing stresses from oxide regions above and below the silicon waveguide contact regions. Based on the above index shift values, a 31.25 μm long phase shifter region is required to achieve a phase shift for the partially-clad waveguide and a shape-memory 3% volume expansion.

Finally, we use the figure of merit approach for estimating $\chi^{(2)}$. The strain gradient-field overlap integral is calculated in COMSOL. Based on the compiled experimental data in [62], we interpolate a shape-memory strain-induced $\chi^{(2)}$ of $\sim$50 pm/V for the above waveguide. Using Equation 5.14, we obtain an estimated $V_\pi L \sim$ 27 V cm.

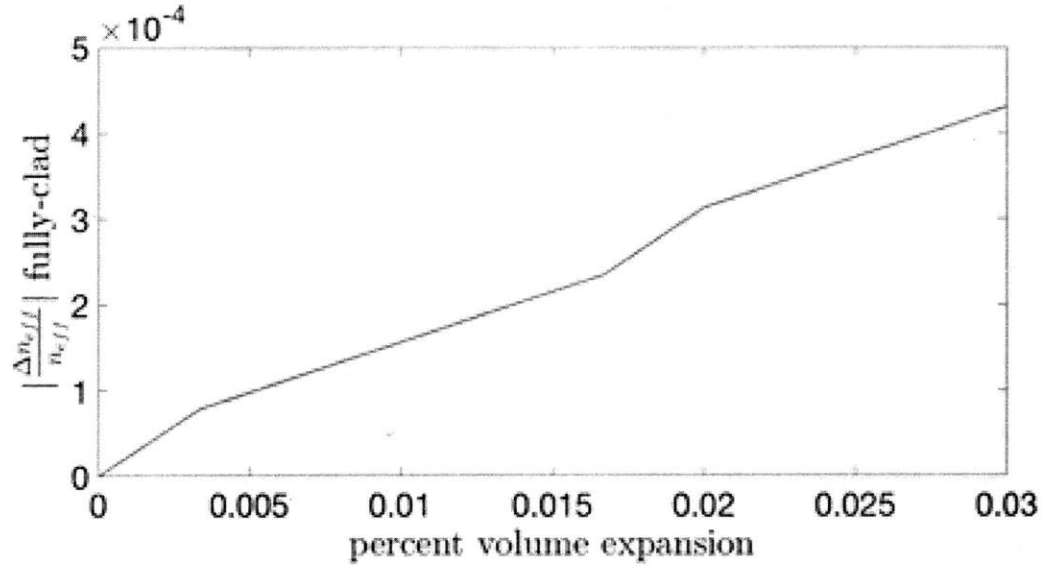

Figure 5.5: Fully oxide-clad waveguide refractive index shift as a function of shape-memory material volume expansion.

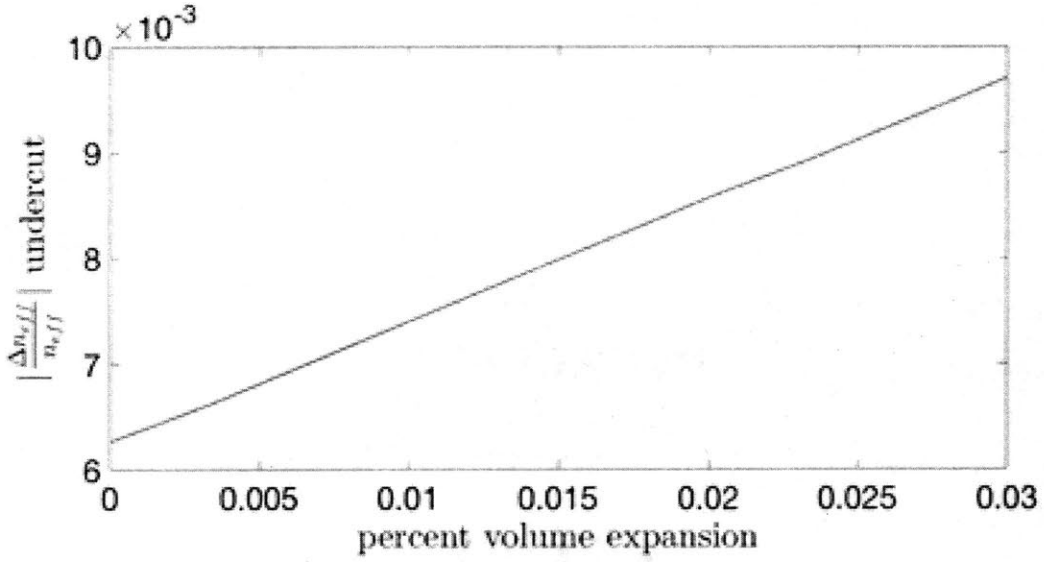

Figure 5.6: Partially oxide-clad waveguide refractive index shift as a function of shape-memory material volume expansion.

Chapter 6

Conclusion

We have presented an *in situ* feedback-controlled protocol for correction of errors in microring resonators for single photon generation. By using the classical pump laser fields to track, diagnose and correct frequency variations, our technique runs in parallel to the quantum computation without making any destructive measurements on the qubits themselves. This approach enables frequency locking of a large number of single photon sources for quantum photonic technologies by distributing a local oscillator across a chip or chip network. In the future, electronic control circuitry could also be integrated on-chip to allow a large number of single photon sources to be frequency-locked to a local oscillator. We have also presented a new approach to implementing strain-actuated phase shifts in silicon waveguides using shape-memory materials.

Bibliography

[1] T. D. Ladd, F. Jelezko, R. Laflamme, Y. Nakamura, C. Monroe, and J. L. O'Brien, Quantum computers, *Nature* **464**, 45–53 (2015).

[2] J. L. O'Brien, A. Furusawa, and J. Vučković, Photonic quantum technologies, *Nat. Photon.* **3**, 687–695 (2009).

[3] Robert Boyd, Nonlinear Optics, Third Edition, Elsevier (2008).

[4] Lukas Chrostowski and Michael Hochberg, Silicon Photonics Design, Cambridge University Press (2015).

[5] N. C. Harris, D. Grassani, A. Simbula, M. Pant, M. Galli, T. Baehr-Jones, M. Hochberg, D. Englund, D. Bajoni, and C. Galland, Integrated source of spectrally filtered correlated photons for large-scale quantum photonic systems, *Phys. Rev. X* **4**, 041047–041010 (2014).

[6] J. Carolan, C. Harrold, C. Sparrow, E. Martín López, N. J. Russell, J. W. Silverstone, P. J. Shadbolt, N. Matsuda, M. Oguma, M. Itoh, G. D. Marshall, M. G. Thompson, J. C. F. Matthews, T. Hashimoto, J. L. O'Brien, and A. Laing, Universal linear optics, *Science* **349**, 711–716 (2015).

[7] F. Najafi, J. Mower, N. C. Harris, F. Bellei, A. Dane, C. Lee, X. Hu, P. Kharel, F. Marsili, S. Assefa, K. K. Berggren, and D. Englund, On-chip detection of non-classical light by scalable integration of single-photon detectors, *Nat. Comms.* **6**, 1–8 (2015).

[8] Felix Eltes, Gerardo E. Villarreal-Garcia, Daniele Caimi, Heinz Siegwart, Antonio A. Gentile, Andy Hart, Pascal Stark et al., An integrated cryogenic optical modulator, arXiv preprint arXiv:1904.10902 (2019).

[9] C. Sun, M. T. Wade, Y. Lee, J. S. Orcutt, L. Alloatti, M. S. Georgas, A. S. Waterman, J. M. Shainline, R. R. Avizienis, S. Lin, B. R. Moss, R. Kumar, F. Pavanello, A. H. Atabaki, H. M. Cook, A. J. Ou, J. C. Leu, Y.-H. Chen, K. Asanović, R. J. Ram, M. A. Popović, and V. M. Stojanović, Single-chip microprocessor that communicates directly using light, *Nature* **528**, 534–538 (2015).

[10] N. C. Harris, G. R. Steinbrecher, M. Prabhu, Y. Lahini, J. Mower, D. Bunandar, C. Chen, F. N. C. Wong, T. Baehr-Jones, M. Hochberg, S. Lloyd, and D. Englund, Quantum transport simulations in a programmable nanophotonic processor, *Nat. Photon.* **11**, 447–452 (2017).

[11] J. Wang, S. Paesani, Y. Ding, R. Santagati, P. Skrzypczyk, A. Salavrakos, J. Tura, R. Augusiak, L. Mančinska, D. Bacco, D. Bonneau, J. W. Silverstone, Q. Gong, A. Acín, K. Rottwitt, L. K. Oxenløwe, J. L. O'Brien, A. Laing, and M. G. Thompson, Multidimensional quantum entanglement with large-scale integrated optics, *Science* **360**, 285–291 (2018).

[12] S. Rahimi-Keshari, M. A. Broome, R. Fickler, A. Fedrizzi, T. C. Ralph, and A. G. White, Direct characterization of linear-optical networks, *Opt. Exp.* **21**, 13450–13459 (2013).

[13] D. Grassani, A. Simbula, S. Pirotta, M. Galli, M. Menotti, N. C. Harris, T. Baehr-Jones, M. Hochberg, C. Galland, M. Liscidini, and D. Bajoni, Energy correlations of photon pairs generated by a silicon microring resonator probed by stimulated four wave mixing, *Sci. Rep.* **6** (2016).

[14] Kelly, R. Barends, A. G. Fowler, A. Megrant, E. Jeffrey, T. C. White, D. Sank et al., Scalable in situ qubit calibration during repetitive error detection, *Physical Review A* **94**(3), 032321 (2016).

[15] Z. Vernon, M. Menotti, C. C. Tison, J. A. Steidle, M. L. Fanto, P. M. Thomas, S. F. Preble, A. M. Smith, P. M. Alsing, M. Liscidini, and J. E. Sipe, Truly unentangled photon pairs without spectral filtering, *Opt. Lett., OL* **42**, 3638–3634 (2017).

[16] P. P. Rohde and T. C. Ralph, Error tolerance of the boson-sampling model for linear optics quantum computing, *Phys. Rev. A* **85**, 022332–022335 (2012).

[17] V. S. Shchesnovich, Sufficient condition for the mode mismatch of single photons for scalability of the boson-sampling computer, *Phys. Rev. A* **89**, 022333–022339 (2014).

[18] L. G. Helt, M. Liscidini, and J. E. Sipe, How does it scale? comparing quantum and classical nonlinear optical processes in integrated devices, *J. Opt. Soc. Am. B* **29**, 2199–2212 (2012).

[19] R. S. Judson and H. Rabitz, Teaching lasers to control molecules, *Phys. Rev. Lett.* **68**, 1500–1503 (1992).

[20] H. Rabitz, R. de Vivie-Riedle, M. Motzkus, and K. Kompa, Whither the future of controlling quantum phenomena? *Science* **288**, 824–828 (2000).

[21] C. Ferrie and O. Moussa, Robust and efficient in situ quantum control, *Phys. Rev. A* **91**, 052306–052308 (2015).

[22] K. Padmaraju, D. F. Logan, T. Shiraishi, J. J. Ackert, A. P. Knights, and K. Bergman, Wavelength locking and thermally stabilizing microring resonators using dithering signals, *Journal of Lightwave Technology* **32**, 505–512 (2013).

[23] F. Horst, W. M. J. Green, S. Assefa, S. M. Shank, Y. A. Vlasov, and B. J. Offrein, Cascaded Mach-Zehnder wavelength filters in silicon photonics for low loss and flat pass-band WDM (de-)multiplexing, *Opt. Exp.* **21**, 11652–11657 (2013).

[24] J. Michel, J. Liu, and L. C. Kimerling, High-performance Ge-on-Si photodetectors, *Nat. Photon.* **4**, 527–534 (2010).

[25] N. C. Harris, Y. Ma, J. Mower, T. Baehr-Jones, D. Englund, M. Hochberg, and C. Galland, Efficient, compact and low loss thermo-optic phase shifter in silicon, *Opt. Exp.* **22**, 10487–10487 (2014).

[26] T. J. Seok, N. Quack, S. Han, R. S. Muller, and M. C. Wu, Large-scale broadband digital silicon photonic switches with vertical adiabatic couplers, *Optica* **3**, 64–67 (2016).

[27] D. J. Thomson, F. Y. Gardes, Y. Hu, G. Mashanovich, M. Fournier, P. Grosse, J.-M. Fedeli, and G. T. Reed, High contrast 40Gbit/s optical modulation in silicon, *Opt. Exp.* **19**, 11507–11516 (2011).

[28] B. E. Little, J.-P. Laine, and S. T. Chu, Surface-roughness-induced contradirectional coupling in ring and disk resonators, *Opt. Lett., OL* **22**, 4–3 (1997).

[29] J. A. Nelder and R. Mead, A simplex method for function minimization, *The Computer Journal* **7**, 308–313 (1965).

[30] Z. Zhou, B. Yin, and J. Michel, On-chip light sources for silicon photonics, *Light Sci. Appl.* **4**, e358 (2015).

[31] M. Piekarek, D. Bonneau, S. Miki, T. Yamashita, M. Fujiwara, M. Sasaki, H. Terai, M. G. Tanner, C. M. Natarajan, R. H. Hadfield, J. L. O'Brien, and M. G. Thompson, High-extinction ratio integrated photonic filters for silicon quantum photonics, *Opt. Lett., OL* **42**, 815–814 (2017).

[32] Z. Wang, H. Liu, Q. Sun, N. Huang, S. Li, and J. Han, The influence of thermal and free carrier dispersion effects on all-optical wavelength conversion in a silicon racetrack-shaped microring resonator, *Laser Phys.* **26**, 075403–8 (2016).

[33] H. Lin, Z. Luo, T. Gu, L. C. Kimerling, K. Wada, A. Agarwal, and J. Hu, Mid-infrared integrated photonics on silicon: a perspective, *Nanophotonics* **7**, 2733–28 (2017).

[34] Y. Zou, S. Chakravarty, C.-J. Chung, X. Xu, and R. T. Chen, Mid-infrared silicon photonic waveguides and devices, *Photon. Res., PRJ* **6**, 254–23 (2018).

[35] A. H. Atabaki, S. Moazeni, F. Pavanello, H. Gevorgyan, J. Notaros, L. Alloatti, M. T. Wade, C. Sun, S. A. Kruger, H. Meng, K. Al Qubaisi, I. Wang, B. Zhang, A. Khilo, C. V. Baiocco, M. A. Popović, V. M. Stojanović, and R. J. Ram, Integrating photonics with silicon nanoelectronics for the next generation of systems on a chip, *Nature* **556**, 349–354 (2018).

[36] L. Carroll, J.-S. Lee, C. Scarcella, K. Gradkowski, M. Duperron, H. Lu, Y. Zhao, C. Eason, P. Morrissey, M. Rensing, S. Collins, H. Hwang, and P. O'Brien, Photonic packaging: transforming silicon photonic integrated circuits into photonic devices, *Applied Sciences* **6**, 426–21 (2016).

[37] C. Schuck, W. H. P. Pernice, and H. X. Tang, Waveguide integrated low noise NbTiN nanowire single-photon detectors with milli-Hz dark count rate, *Sci. Rep.* **3**, 696–6 (2013).

[38] E. Schelew, M. K. Akhlaghi, and J. F. Young, Waveguide integrated superconducting single-photon detectors implemented as near-perfect absorbers of coherent radiation, *Nat. Comms.* **6**, 1–8 (2015).

[39] D. Zhu, Q.-Y. Zhao, H. Choi, T.-J. Lu, A. E. Dane, D. Englund, and K. K. Berggren, A scalable multi-photon coincidence detector based on superconducting nanowires, *Nature Nanotechnology* **13**, 596–601 (2018).

[40] M. Heuck, M. Pant, and D. R. Englund, Temporally and spectrally multiplexed single photon source using quantum feedback control for scalable photonic quantum technologies, *New J. Phys.* **20**, 063046–14 (2018).

[41] M. Pant, H. Krovi, D. Englund, and S. Guha, Rate-distance tradeoff and resource costs for all-optical quantum repeaters, *Phys. Rev. A* **95**, 012304–14 (2017).

[42] Terry Rudolph, Why I am optimistic about the silicon-photonic route to quantum computing, *APL Photonics* **2**(3), 030901 (2017).

[43] Pieter Kok, William J. Munro, Kae Nemoto, Timothy C. Ralph, Jonathan P. Dowling, and Gerard J. Milburn, Linear optical quantum computing with photonic qubits, *Reviews of Modern Physics* **79**(1), 135 (2007).

[44] R. Santagati, J. W. Silverstone, M. J. Strain, M. Sorel, S. Miki, T. Yamashita, M. Fujiwara, M. Sasaki, H. Terai, M. G. Tanner, C. M. Natarajan, R. H. Hadfield, J. L. O'Brien, and M. G. Thompson, Silicon photonic processor of two-qubit entangling quantum logic, *Journal of Optics*, **19**(11), 114006 (2017).

[45] Wim Bogaerts, Peter De Heyn, Thomas Van Vaerenbergh, Katrien De Vos, Shankar Kumar Selvaraja, Tom Claes, Pieter Dumon, Peter Bienstman, Dries Van Thourhout, and Roel Baets, Silicon microring resonators, *Laser & Photonics Reviews*, **6**(1), 47-73 (2012).

[46] Joshua W. Silverstone, Damien Bonneau, Jeremy L. O'Brien, and Mark G. Thompson, Silicon quantum photonics, *IEEE Journal of Selected Topics in Quantum Electronics*, **22**(6), 390-402 (2016).

[47] Damien Bonneau, Joshua W. Silverstone, and Mark G. Thompson, Silicon quantum photonics, in Silicon Photonics III, pages 41-82, Springer, Berlin, Heidelberg (2016).

[48] Imad I. Faruque, Gary F. Sinclair, Damien Bonneau, John G. Rarity, and Mark G. Thompson, On-chip quantum interference with heralded photons from two

independent micro-ring resonator sources in silicon photonics, *Optics Express*, **26**(16), 20379-20395 (2018).

[49] Jacques Carolan, Uttara Chakraborty, Nicholas C. Harris, Mihir Pant, Tom Baehr-Jones, Michael Hochberg, and Dirk Englund, Scalable feedback control of single photon sources for photonic quantum technologies, *Optica*, **6**(3), 335-340 (2019).

[50] J. W. Silverstone, D. Bonneau, K. Ohira, N. Suzuki, H. Yoshida, N. Iizuka, M. Ezaki, C. M. Natarajan, M. G. Tanner, R. H. Hadfield, V. Zwiller, G. D. Marshall, J. G. Rarity, J. L. O'Brien, and M. G. Thompson, On-chip quantum interference between silicon photon-pair sources, *Nature Photonics*, **8**(2), 104 (2014).

[51] J. W. Silverstone, R. Santagati, D. Bonneau, M. J. Strain, M. Sorel, J. L. O'Brien, and M. G. Thompson, Qubit entanglement between ring-resonator photon-pair sources on a silicon chip, *Nature Communications*, **6**, 7948 (2015).

[52] Xiaogang Qiang, Xiaoqi Zhou, Jianwei Wang, Callum M. Wilkes, Thomas Loke, Sean O'Gara, Laurent Kling, Graham D. Marshall, and J.B. Wang, Large-scale silicon quantum photonics implementing arbitrary two-qubit processing, *Nature Photonics*, **12**(9), 534 (2018).

[53] Xiao Mei Zeng, Zehui Du, Nobumichi Tamura, Qing Liu, Christopher A. Schuh, and Chee Lip Gan, In-situ studies on martensitic transformation and high-temperature shape memory in small volume zirconia, *Acta Materialia*, **134**, 257-266 (2017).

[54] Xiao Mei Zeng, Zehui Du, Christopher A. Schuh, Nobumichi Tamura, and Chee Lip Gan, Microstructure, crystallization and shape memory behavior of titania and yttria co-doped zirconia, *Journal of the European Ceramic Society* **36**(5), 1277-1283 (2016).

[55] Rune S. Jacobsen, Karin N. Andersen, Peter I. Borel, Jacob Fage-Pedersen, Lars H. Frandsen, Ole Hansen, Martin Kristensen et al., Strained silicon as a new electro-optic material, *Nature* **441**(7090), 199 (2006).

[56] Peter C. Humphreys, Benjamin J. Metcalf, Justin B. Spring, Merritt Moore, Patrick S. Salter, Martin J. Booth, W. Steven Kolthammer, and Ian A. Walmsley, Strain-optic active control for quantum integrated photonics, *Optics Express* **22**(18), 21719-21726 (2014).

[57] Bartos Chmielak, Michael Waldow, Christopher Matheisen, Christian Ripperda, Jens Bolten, Thorsten Wahlbrink, Michael Nagel, Florian Merget, and Heinrich Kurz, Pockels effect based fully integrated, strained silicon electro-optic modulator, *Optics Express* **19**(18) 17212-17219 (2011).

[58] Bartos Chmielak, Christopher Matheisen, Christian Ripperda, Jens Bolten, Thorsten Wahlbrink, Michael Waldow, and Heinrich Kurz, Investigation of local strain distribution and linear electro-optic effect in strained silicon waveguides, *Optics Express* **21**(21), 25324-25332 (2013).

[59] Costanza Lucia Manganelli, Paolo Pintus, and Claudio Bonati, Modeling of strain-induced Pockels effect in Silicon, *Optics Express* **23**(22), 28649-28666 (2015).

[60] Y. Sebbag, Y., I. Goykhman, B. Desiatov, T. Nachmias, O. Yoshaei, M. Kabla, S. E. Meltzer, and U. Levy, Silicon optical phase shifter based on strain induced by a piezoelectric PZT thin film, in CLEO: Science and Innovations, pp. CTh1C-3, Optical Society of America (2012).

[61] Chong-Ki Hong, Zhe-Yu Ou, and Leonard Mandel, Measurement of subpicosecond time intervals between two photons by interference, *Physical Review Letters* **59**(18), 2044 (1987).

[62] Seyed A. Aleali, Modeling of Strain Induced Pockels Effect in Silicon Photonic Waveguides, Master's Thesis, Department of Electronics, Carleton University, Ottawa, Canada (2014).

[63] Adil Masood, Marianna Pantouvaki, Guy Lepage, Peter Verheyen, Joris Van Campenhout, Philippe Absil, Dries Van Thourhout, and Wim Bogaerts, Comparison of heater architectures for thermal control of silicon photonic circuits, in The 10th International Conference on Group IV Photonics, pp. 83-84, IEEE (2013).

[64] Takumi Moriyama, Daiki Tanaka, Paridhi Jain, Hitoshi Kawashima, Masashi Kuwahara, Xiaomin Wang, and Hiroyuki Tsuda, Ultra-compact, self-holding asymmetric Mach-Zehnder interferometer switch using Ge2Sb2Te5 phase-change material, *IEICE Electronics Express* **11**(15), 20140538-20140538 (2014).

[65] Hamed Sattari, Teodoro Graziosi, Marcell Kiss, Tae Joon Seok, Sangyoon Han, Ming C. Wu, and Niels Quack, Analog silicon photonic MEMS phase-shifter with double-step electrostatic actuation, in Proceedings of the 2017 IEEE International Conference on Optical MEMS and Nanophotonics, Santa Fe, NM (2017).

[66] Graham T. Reed, and CE Jason Png, Silicon optical modulators, *Materials Today* **8**(1), 40-50 (2005).

[67] Clemens Schriever, Christian Bohley, Jörg Schilling, and Ralf B. Wehrspohn, Strained silicon photonics, *Materials* **5**(5), 889-908 (2012).

[68] Uttara Chakraborty, Jacques Carolan, Yifei Zhang, Juejun Hu, and Dirk Englund, Schemes for non-volatile phase shifters for large-scale photonic integrated circuits based on phase-change and shape-memory materials, MRS Fall Meeting and Exhibit (Session EP04.07), Boston, MA, November 25-30, 2018.

[69] Rui Tang, Toward 4-photon generation on a silicon chip, MIT Quantum Photonics Lab Internal Group Meeting (2019).

[70] G. Z. Mashanovich, M. Milosevic, P. Matavulj, S. Stankovic, B. Timotijevic, P. Y. Yang, E. J. Teo, M. B. H. Breese, A. A. Bettiol, and G. T. Reed, Silicon photonic waveguides for different wavelength regions, *Semiconductor Science and Technology* **23**(6), 064002 (2008).